buildings

MDPI

Article

Thermo-Mechanical Resilience and Sustainability of Steel Fiber-Reinforced Mortars with High-Volume Fly Ash Under Extreme Conditions

Murteda Ünverdi, Selin Özteber, Ali Mardani *, Kemal Karakuzu and Sultan Husein Bayqra

Department of Civil Engineering, Faculty of Engineering, Bursa Uludag University, 16059 Bursa, Turkey; murtedaunverdi@uludag.edu.tr (M.Ü.); ozteberselin@uludag.edu.tr (S.Ö.); karakuzu.kemal@gmail.com (K.K.); sultanhuseinbayqra1050@gmail.com (S.H.B.)

* Correspondence: alimardani@uludag.edu.tr

Abstract

Developing sustainable and fire-resistant infrastructure is a critical technological, economic, and environmental challenge for modern construction stakeholders. Traditional cementitious composites experience severe microstructural degradation under extreme temperatures and their high carbon footprint exacerbates global environmental concerns. While the individual high-temperature behaviors of supplementary cementitious materials and fibers have been widely studied, the long-term synergistic mechanisms of high-volume fly ash combined with steel fibers under extreme thermal shock remain critically underinvestigated. To address this urgent need and bridge this scientific gap, hybrid mortars incorporating high-volume fly ash (FA) and steel fibers (SF) were tested under prolonged curing (150 days) and extreme heat (up to 600 °C). In terms of engineering and construction effects, the optimal CFA50-F hybrid composite delivered the highest residual compressive and flexural capacities (retaining nearly 60% of its late-age compressive strength at 32.00 MPa), preserved acoustic continuity (restricting UPV loss to 41.4%), and severely restricted high-temperature capillary permeability (limiting the water absorption increase to 49.7%) compared to traditional plain matrices. Scientifically, this superior resistance is governed by a two-step protective mechanism. High-volume FA chemically stabilizes the matrix by consuming vulnerable portlandite and preventing the formation of expansive calcium oxide. Simultaneously, ultra-fine FA particles physically densify the interfacial transition zones, securely anchoring the steel fibers and preventing premature high-temperature pull-out, while enabling the fibers to bridge thermally induced macro-cracks successfully. Environmentally and economically, an annualized service-life Life Cycle Assessment (LCA) revealed that substituting 50% of the cement with FA completely subsidizes the production-stage carbon penalty of the metallic reinforcement. By extending the operational lifespan to 40 years, the CFA50-F composite achieves a net 27% reduction in annualized global warming potential, providing a highly sustainable and cost-effective material solution.

Keywords: thermo-mechanical resilience; steel fiber-reinforced mortar; high-volume fly ash; explosive spalling; interfacial transition zone (ITZ); ultrasonic pulse velocity (UPV); life cycle assessment (LCA)

Check for updates

Academic Editors: Dianchao Wang, Bochao Sun, Fubin Zhang, Chang Sun, Gaoyu Liao and Nanqiao You

Received: 29 March 2026
Revised: 25 April 2026
Accepted: 26 April 2026
Published: 29 April 2026

Copyright: © 2026 by the authors. Licensee MDPI, Basel, Switzerland. This article is an open access article distributed under the terms and conditions of the Creative Commons Attribution (CC BY) license.

1. Introduction

Cementitious composites frequently encounter elevated temperatures during fire events or specific industrial applications, leading to a severe deterioration of mechanical

properties and structural integrity [1,2]. Thermal exposure causes internal moisture evaporation, pore pressure accumulation, and subsequent explosive spalling in the matrix [3,4]. The degradation mechanism under extreme heat is heavily linked to the irreversible decomposition of primary hydration products [5]. High-temperature environments accelerate the coarsening of the pore structure and induce severe micro-cracking due to the thermal incompatibility between the cementitious paste and the aggregates [6]. Consequently, the load-bearing capacity of structural elements diminishes rapidly, necessitating the development of temperature-resistant binder modifications [7].

Beyond thermal exposure, the long-term durability of cementitious composites is fundamentally challenged by various aggressive environmental conditions. Chemical deterioration, particularly chloride penetration and sulfate attack, severely compromises structural integrity. Chloride ions penetrate the pore network, triggering the corrosion of internal steel reinforcement, which leads to concrete spalling and sudden mechanical failure [8,9]. Sulfate ions react with the cement matrix to form delayed ettringite and gypsum, inducing massive internal swelling pressures and extensive micro-cracking [10–12]. Physical weathering also significantly accelerates degradation. Successive freezing and thawing cycles generate internal hydraulic pressures as pore water expands, resulting in progressive structural fracturing and macro/micro-crack propagation [13–15]. Alternating wetting and drying cycles exacerbate crack propagation by imposing repeated shrinkage strains and accelerating aggressive ion transport [16]. These diverse degradation pathways show that preserving the mechanical properties of composites strictly depends on refining the pore structure and mitigating internal expansion stresses.

Upon exposure to temperatures exceeding 400 °C, portlandite (calcium hydroxide, CH) within the cement matrix dehydrates into calcium oxide (CaO) [17,18]. During the cooling phase, the highly reactive CaO absorbs ambient moisture and rehydrates, triggering localized volume expansions of up to 44%, which produces extensive micro-cracking and eventual structural failure [19,20]. Researchers utilizing non-destructive testing methods, such as ultrasonic pulse velocity (UPV) and water absorption measurements, have documented the severe internal damage network caused by these expansive forces [21,22]. The decrease in UPV values is particularly indicative of increased porosity and the propagation of macroscopic cracks throughout the matrix [23]. Mitigating this phase transformation is critical to maintaining the matrix's residual integrity upon cooling.

To control thermal damage, supplementary cementitious materials (SCMs) are incorporated into the concrete to consume the vulnerable CH phase. Fly ash (FA) is highly effective due to its pozzolanic activity, chemically converting CH into secondary calcium silicate hydrate (C-S-H) gels [24–28]. High-volume FA mixtures exhibit superior thermal stability because the reduced CH content minimizes the expansive CaO formation during the cooling phase [29–32]. The successful application of various industrial by-products further supports the strategy of modifying the binder matrix for thermal endurance [33–36]. The secondary hydration products generated by FA not only refine the capillary voids but also exhibit higher thermal stability than the primary hydration phases [37–39]. However, at extreme temperatures exceeding 600 °C, even these secondary gels begin to decompose, rendering chemical modification alone insufficient to prevent brittle failure [40].

Despite the chemical stability provided by FA, cementitious matrices remain inherently brittle and susceptible to rapid crack propagation under thermal shock. Steel fibers (SF) are frequently integrated into mixtures to provide physical reinforcement and bridge macrocracks [41–43]. The inclusion of SF effectively delays crack initiation, transfers tensile stresses across crack surfaces, and preserves the flexural capacity of the composite at elevated temperatures [23,44–46]. Experimental data repeatedly confirm that SF mitigates explosive spalling and enhances the residual compressive toughness of the matrix [47–51].

The high melting point of steel ensures that the fibers maintain their structural bridging capabilities well beyond the decomposition temperatures of the cementitious matrix. This bridging mechanism redistributes internal stresses and provides a confining effect, thereby preserving the residual bearing capacity of the structural element.

While the independent effects of FA and SF are well documented, the synergistic mechanisms of HVFA combined with SF under extreme thermal loads remain underinvestigated. Existing literature primarily focuses on lower FA substitution rates or purely mechanical assessments without tracking physical degradation indicators over prolonged curing periods [52–56]. The combined physical crack-bridging of SF and the chemical CH-depletion by FA creates a hybrid resistance mechanism that alters the internal porosity and acoustic impedance of the material [57–61]. Correlating mechanical strength losses with non-destructive physical parameters such as UPV and water absorption for hybrid HVFA-SF systems up to 150 days of curing and 600 °C remains a distinct gap in the literature [34,62,63]. Evaluating extended curing regimes is vital because the pozzolanic reactions of high-volume FA are time-dependent and significantly alter the matrix density. A comprehensive assessment linking long-term hydration, multi-scale structural damage, and acoustic non-destructive evaluations will provide a holistic understanding of this synergistic thermal protection. A summary of previous studies investigating the behavior of various fiber-reinforced cementitious composites exposed to elevated temperatures is presented in Table 1.

Table 1. Summary of previous studies.

Reference	Binder/Matrix Type	Fiber Type	Maximum Temperature (°C)	Key Findings
[39]	HPC with Fly Ash/Slag	-	800	Highlighted that high-volume pozzolanic concretes perform better in retaining residual compressive strength compared to pure OPC up to 600 °C.
[64]	Cement Mortar (Pumice Agg.)	-	900	Demonstrated that 60% FA replacement limits strength loss effectively by creating a stronger aggregate-paste transition zone.
[4]	Cement Mortar	Steel, PVA, GF, PP	650	Found that steel fibers effectively prevented explosive spalling and provided high residual flexural capacity compared to polymer fibers.
[65]	High-Strength Fly Ash Concrete	Steel	800	Confirmed that the high melting point of steel fibers significantly enhances strength retention in HVFA concretes during extreme thermal exposure.
[56]	Cement Mortar	Steel, PVA, Whisker	800	Indicated that multi-scale hybrid fibers (steel+PVA) significantly restrain crack propagation, improving compressive toughness at high temperatures.
[58]	Concrete with FA & Slag	Steel, PVA	800	Showed that steel fibers are highly effective at bridging macro-cracks, while PVA controls early-age shrinkage, creating a ductile failure mechanism.
[6]	Ultra-High Performance Concrete	Steel, Flax	800	Concluded that the synergistic use of steel and flax fibers completely prevents spalling and maintains mechanical strength by releasing vapor pressure.

Table 1. *Cont.*

Reference	Binder/Matrix Type	Fiber Type	Maximum Temperature (°C)	Key Findings
[66]	Geopolymer Mortar (FA/Slag)	-	800	Established that FA-based binders maintain thermal stability and experience a dynamic elasticity modulus recovery up to a certain high temperature limit.
[23]	Self-Compacting Concrete	Steel, PP, Glass	600	Revealed that steel fibers prevent crack propagation and limit UPV reduction more effectively than PP fibers at 600 °C.
[40]	Cement-Based Composites	Steel, Basalt	800	Reported that higher FA substitution rates combined with hybrid fibers drastically minimize thermal degradation and microstructure coarsening.
[47]	Ultra-High Performance Concrete	Steel, PE, Whisker	800	Showed that multi-scale fibers alleviate the cracking degree, reducing internal pore pressure and preserving residual modulus of elasticity.
[59]	High-Strength Concrete	Micro Steel Fiber	800	Documented that micro steel fibers limit concrete density loss and preserve up to 32% more residual tensile strength than control mixes.
[21]	Cement Mortar (Mineral Admix)	Basalt	800	Highlighted the strong correlation between residual compressive strength and UPV results after heating, proving mineral admixtures' void-filling effect.
[19]	Concrete	Waste Steel Fiber	800	Found that steel fiber addition preserves the matrix integrity, though UPV values drop sharply after 600 °C due to void formation and crack widening.
[67]	Silica Fume Based AAMs	Steel	1000	Demonstrated that 1% steel fiber prevents thermal cracking efficiently, stabilizing water absorption and limiting UPV drop after 1000 °C exposure.

Note: HPC: High-Performance Concrete; OPC: Ordinary Portland Cement; PVA: Polyvinyl Alcohol; GF: Glass Fiber; PP: Polypropylene; PE: Polyethylene; AAMs: Alkali-Activated Materials; UHPC: Ultra-High Performance Concrete.

As seen in the comprehensive literature review (Table 1), a dual scientific problem remains critically unresolved. First, from a fundamental research perspective, there is a significant lack of long-term experimental studies evaluating the synergistic mechanisms of high-volume fly ash in steel fiber-reinforced mortars under extreme conditions, particularly regarding progressive microstructural degradation and acoustic impedance. Second, there is a distinct scientific deficit in the form of inadequate practical engineering solutions; the construction industry urgently requires scalable, highly resilient, and low-carbon material designs to address these thermal risks in real-world construction. To bridge these theoretical and applied gaps, this study aims to investigate the physical and mechanical properties of mortar mixtures incorporating 30% and 50% FA replacement levels and 1% volumetric SF addition. Specimens were cured for 28, 56, and 150 days and subsequently subjected to 20 °C, 300 °C, and 600 °C environments. Compressive strength, flexural strength, UPV, and water absorption capacities were measured to evaluate the synergistic protective effect of FA and SF against thermal degradation. The empirical findings aim to

elucidate the mechanisms by which chemical CH depletion and physical crack bridging interact to resist thermal shock. The experimental procedure, including mixture preparation, curing periods, and thermal exposure regimes, is illustrated in Figure 1. Ultimately, the correlations derived between destructive and non-destructive parameters will offer practical insights for designing highly durable cementitious composites for high-temperature real-world applications.

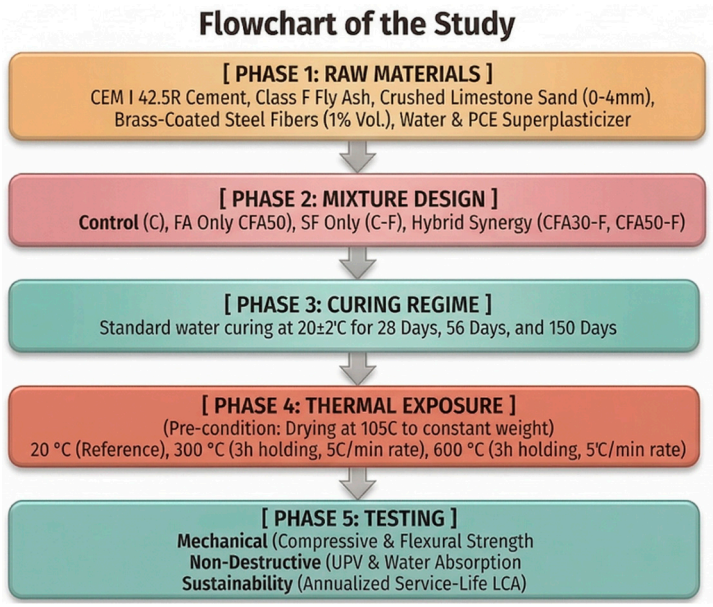


Figure 1. Flowchart of the study.

2. Materials and Methods

CEM I 42.5R Portland cement (supplied by Bursa-Beton Inc., Bursa, Turkey) complying with EN 197-1 [68] and class F FA (obtained from Orhaneli Thermal Power Plant, Bursa, Turkey) conforming to ASTM C618 [69] was utilized as a binder. Some physical, chemical, and mechanical properties provided by the manufacturer are shown in Table 2.

Table 2. Physical, chemical, and mechanical properties of binders.

(%)	Cement	FA	Physical Properties		Cement	FA
SiO_2	18.86	48.21	Specific gravity C_2S (%) C_3A (%) C_4AF (%)		3.15	2.12
Al_2O_3	5.71	19.33				
Fe_2O_3	3.09	8.88		1-day	14.7	-
CaO	62.7	8.47	Compressive strength	2-day	26.8	-
MgO	1.16	6.23	(MPa)	7-day	49.8	-
SO_3	2.39	0.17		28-day	58.5	-
$Na_2O + 0.658\ K_2O$	0.92	1.40				
Cl^-	0.01		Specific surface (cm^2/g)		3530	4300
Insoluble residue	0.32		0.045 mm remaining on sieve (g) (%)		7.6	10
Loss of ignition	3.2		Pozzolanic activity	28-day	-	77.7
Free CaO	1.26		index (%)	90-day	-	91.3

Crushed limestone sand passed through a 4 mm sieve was used as aggregate. The specific gravity and water absorption values of the aggregate were found to comply with the EN 1097-1 [70] and were obtained as 2.68 and 1%, respectively. The sieve analysis of the aggregate is shown in Table 3.

Table 3. Sieve analysis of aggregate used in mixtures.

Sieve Size (mm)	Passing (%)	Residual (%)
4.00	100	0
2.00	77.5	22.5
1.00	49.4	50.7
0.50	32.0	68.0
0.25	12.9	87.1
0.125	2.5	97.5

In the fiber-reinforced mixtures, brass-coated SF (manufactured by DRACO, Istanbul, Turkey) with a length of 12 mm and a diameter of 0.18 mm was utilized at 1% of the total mixture volume. The primary physical and mechanical properties of the SF, as provided by the manufacturer, are summarized in Table 4. Furthermore, Figure 2 illustrates the raw materials (cement, fly ash, and SF) used in this study, along with the sequential stages of sample production, molding, and high-temperature furnace placement.

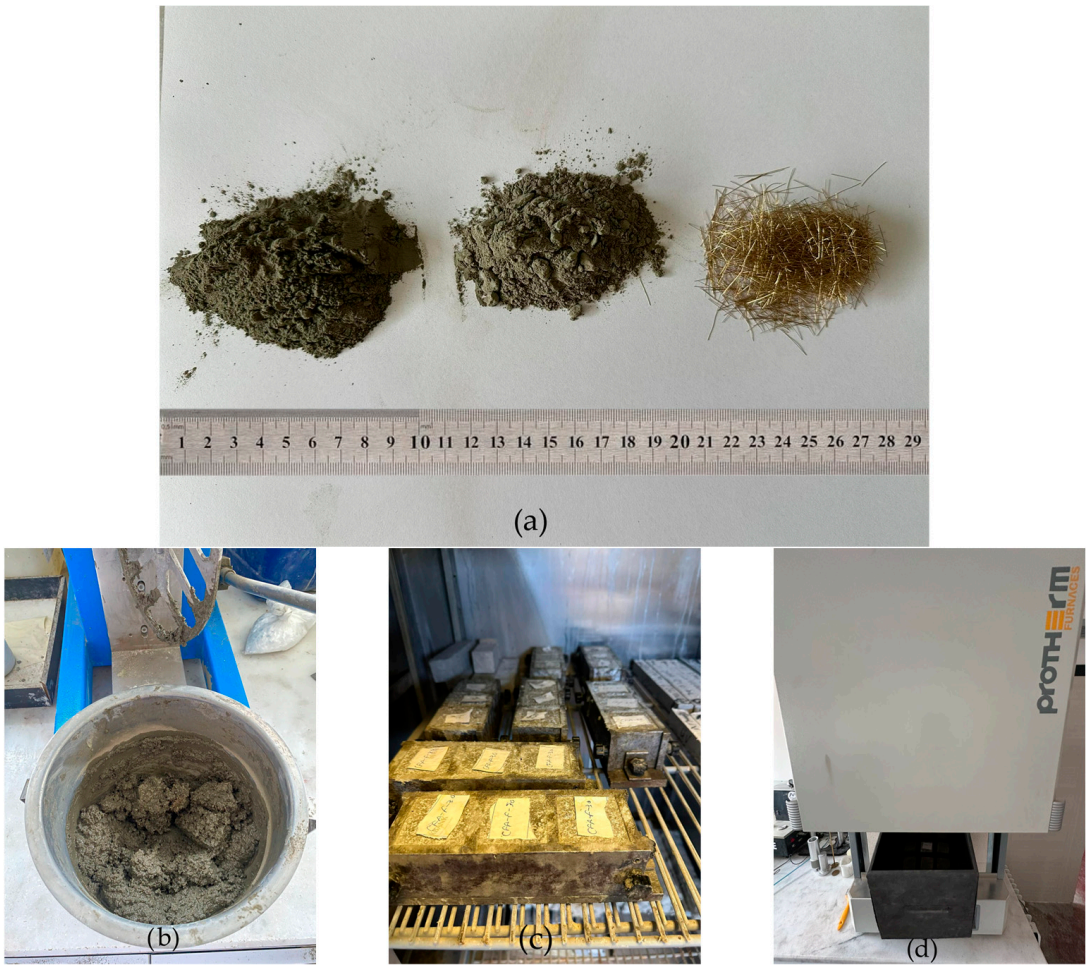


Figure 2. (**a**) Cement, fly ash, and SF used in the study, (**b**) sample production, (**c**) molding, (**d**) placement in high-temperature furnace.

Table 4. Some physical and mechanical properties of SF.

Type	Slenderness Ratio	Length (mm)	Diameter (mm)	Tensile Strength (N/mm^2)
Brass-coated SF	1.08	12	0.18	2000

The mortar mixtures were prepared in accordance with ASTM C109 [71], and the water/binder and sand/binder ratios were kept constant at 0.485 and 2.75, respectively. The complete experimental formulation program, detailing the material proportions used to prepare the mortar mixtures, is shown in Table 5. The flow value of the mortar mixtures produced was determined in accordance with ASTM C1437 [72]. Slump-flow values were set at 250 ± 20 mm for all mixtures. To achieve the target slump-flow, polycarboxylate ether-based high-range water-reducing admixture (HRWRA) was used at various ratios. Some features of the HRWRA provided by the manufacturer are given in Table 6. The mixtures were coded based on binder composition, steel fiber inclusion, and exposure temperature. The plain control mixture is denoted as "C". The inclusion of fly ash is represented by "FA" followed by its mass replacement percentage (e.g., CFA30 and CFA50). The addition of 1% volumetric steel fibers is indicated by the letter "F" (e.g., CF, CFA30-F, and CFA50-F). Finally, for the high-temperature tests, the exposure temperature is appended to the base code (e.g., CFA50-F 600 °C).

Table 5. The mix proportions and flow values.

Mixture Group	Cement	Water	FA	SF	Aggregate (0–4 mm)	HRWRA	Slump-Flow Value (mm)
C	1	0.485	-	-	2.75	0.004	250
CFA30	0.7	0.485	0.3	-	2.75	0.0036	248
CFA50	0.5	0.485	0.5	-	2.75	0.0035	250
CF	1	0.485	-	0.142	2.75	0.005	240
CFA30-F	0.7	0.485	0.3	0.142	2.75	0.0036	248
CFA50-F	0.5	0.485	0.5	0.142	2.75	0.0035	250

Table 6. Some properties of the HRWRA.

Type	Density (g/cm^3)	pH Value	Chloride Content (%)	Alkali Content Na_2O (%)
Polycarboxylate ether-based	1.023–1.063	5–8	<0.1	<10

The mixtures, prepared to conform to ASTM C109 [71], were placed in molds in accordance with the relevant standard and kept in a curing cabinet at 20 ± 2 °C and 95% relative humidity for 24 h. After 24 h, the specimens were removed from the molds and cured in the lime-saturated standard curing pool at 20 ± 2 °C until the experiment day. The high-temperature effect was applied to 28, 56, and 150-day specimens. In this context, after the specimens were removed from the curing pool on the day of the experiment, they were left to dry at 105 °C until reaching constant weight (verified by consecutive mass measurements taken 2 h apart, showing a mass difference of less than 0.1%). This initial pre-drying step was essential to eliminate free capillary water and standardize the initial moisture state of all specimens. By removing the highly variable influence of free moisture, this procedure ensured that the subsequent extreme-thermal-exposure tests accurately isolated the intrinsic thermochemical degradation of the matrix (e.g., C-S-H dehydration and CH decomposition) from arbitrary steam-induced spalling. The specimens were then

subjected to high temperatures for 3 h after achieving the test temperatures of 300 °C and 600 °C, with a rate of rise of 5 °C/min in the ash furnace (Figure 3).

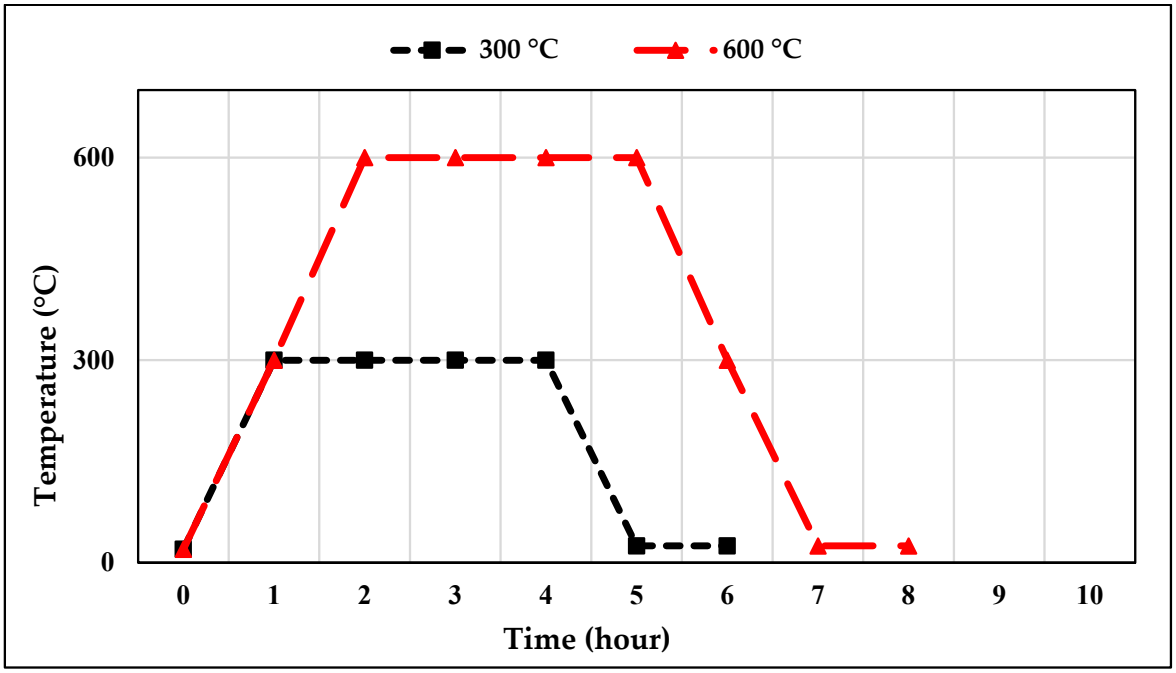


Figure 3. Heating-cooling period of mortar specimens.

To ensure precise reproducibility and statistical reliability, three replicate specimens were tested for each mixture, curing age, and temperature condition, and the average values were reported for all experimental results. The subsequent experimental evaluations followed a systematic step-by-step procedure. First, compressive strength tests were performed on the high-temperature-exposed 50 × 50 × 50 mm cubic specimens according to ASTM C109 [71] standard using a universal testing machine. Second, the flexural strength of the mixtures was determined on 56-day 40 × 40 × 160 mm prismatic specimens according to EN 196-1 [73] using a single-point bending setup. The 56-day curing age was specifically selected for flexural evaluation because it represents an optimal intermediate maturity where the delayed pozzolanic reactions of high-volume fly ash sufficiently densify the fiber-matrix interface, providing a reliable measure of crack-bridging performance while optimizing the limited high-temperature furnace capacity required for the larger prismatic specimens. For non-destructive physical assessments, UPV experiments were conducted on the 28, 56, and 150-day specimens in accordance with ASTM C597 [74] standard, utilizing a direct transmission method with transducers placed on opposite longitudinal faces. Finally, the water absorption (WA) capacity of the hardened mixtures was determined following ASTM C642 [75] standard. Specimens were initially oven-dried at 105 °C until a constant mass was reached, weighed, and subsequently immersed in water until fully saturated to measure the permeable capillary void network.

3. Results and Discussion

The comprehensive experimental outcomes, encompassing CS, UPV, FS, and WAC of all mortar mixtures cured at 28, 56, and 150 days and subsequently exposed to 20 °C, 300 °C, and 600 °C, are systematically summarized in Table 7.

Table 7. Experimental results of the study.

Mixtures	Compressive Strength (MPa)			Ultrasonic Pulse Velocity (m/s)			Flexural Strength (MPa)	Water Absorption (%)		
	28-Day	56-Day	150-Day	28-Day	56-Day	150-Day	56-Day	28-Day	56-Day	150-Day
C-20 °C	62.26	65.71	69.92	4022	4232	4526	5.91	6.50	6.30	6.10
C-300 °C	43.44	43.25	43.96	3472	3597	3678	3.55	7.57	7.43	7.47
C-600 °C	16.63	19.17	23.12	2165	2183	2226	1.72	10.10	9.96	9.82
CFA30-20 °C	45.01	52.16	60.52	4008	4115	4386	5.61	6.20	5.90	5.60
CFA30-300 °C	28.81	33.38	39.20	3472	3731	3926	3.21	7.19	6.56	6.30
CFA30-600 °C	22.10	26.08	27.60	2232	2346	2518	1.90	9.50	8.94	8.46
CFA50-20 °C	38.50	46.50	56.50	3980	4080	4320	5.30	6.40	6.00	5.50
CFA50-300 °C	24.00	29.00	36.50	3450	3760	4000	3.00	7.42	6.56	5.99
CFA50-600 °C	22.00	26.00	29.00	2300	2450	2580	2.05	9.64	8.88	8.16
CF-20 °C	55.38	59.00	66.87	4310	3800	4425	6.49	6.80	6.60	6.40
CF-300 °C	42.38	46.61	56.80	3597	3597	3650	3.72	8.15	7.02	7.75
CF-600 °C	27.01	30.09	30.56	2137	2192	2281	2.10	10.91	9.95	10.12
CFA30-F-20 °C	41.00	47.50	58.50	4170	4300	4550	6.20	6.60	6.30	6.00
CFA30-F-300 °C	32.50	38.00	47.50	3550	3800	4000	3.80	7.78	7.18	6.87
CFA30-F-600 °C	24.00	28.00	32.00	2300	2450	2600	2.30	10.15	9.55	9.09
CFA50-F-20 °C	34.50	42.00	53.50	4180	4280	4520	6.00	6.70	6.40	5.90
CFA50-F-300 °C	27.00	33.50	44.00	3520	3820	4050	3.60	7.97	7.23	6.64
CFA50-F-600 °C	24.00	28.50	32.00	2350	2500	2650	2.40	10.22	9.59	8.83

3.1. Pozzolanic Reaction and Age Effect at Ambient Temperature (20 °C)

The evolution of compressive strength and the internal integrity of the mixtures cured at the reference ambient temperature (20 °C) are illustrated in Figure 4.

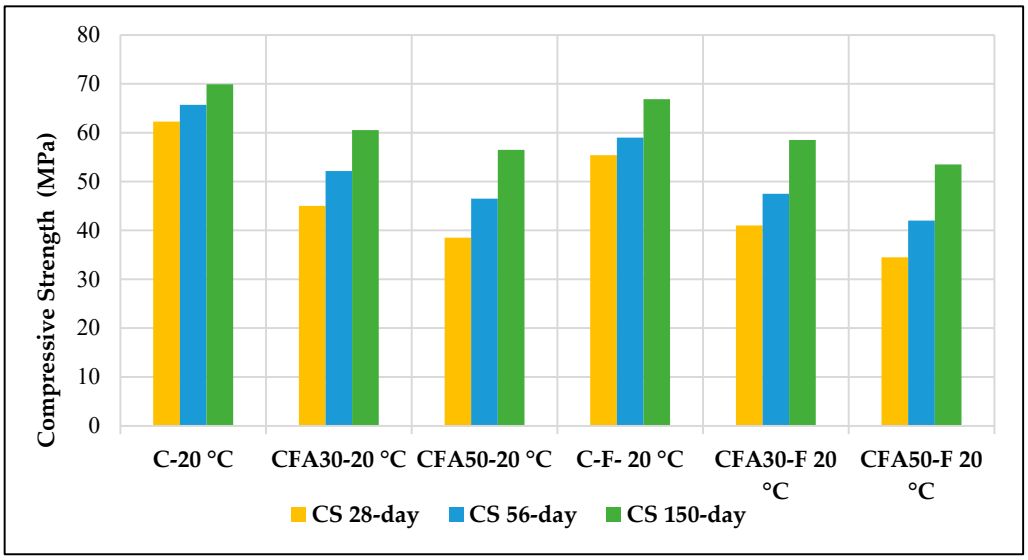


Figure 4. Development of compressive strength of mixtures at 20 °C over 150 days of curing.

At the curing age of 28 days, substituting Portland cement with 30% and 50% high-volume FA induced a substantial reduction in the initial compressive strength. Specifically, while the control (C) mixture achieved 62.26 MPa, the CFA30 and CFA50 specimens exhibited pronounced strength deficits of 27.7% (45.01 MPa) and 38.2% (38.50 MPa), respectively. The paste-dilution effect fundamentally governs this age-strength impairment. During early hydration at ambient conditions, Portland cement generates primary calcium silicate hydrate (C-S-H) gels and liberates calcium hydroxide ($Ca(OH)_2$). FA, heavily reliant on the presence of this liberated CH to activate its amorphous silica and alumina phases,

exhibits highly sluggish secondary hydration kinetics at 28 days, preventing immediate microstructural compaction [67].

Evaluating the mechanical evolution up to 150 days, however, exposes the profound long-term efficiency of these delayed pozzolanic reactions. While the control mixture demonstrated a marginal strength growth of merely 12.3% from 28 to 150 days (reaching 69.92 MPa), the FA-modified matrices underwent extraordinary late-age densification. The CFA30 and CFA50 mixtures achieved remarkable increases in compressive strength of 34.5% and 46.8%, respectively, over the extended curing period. Consequently, the drastic initial strength gap between the extreme CFA50 mix and the plain control significantly narrowed from 38.2% to a highly tolerable 19.2% at 150 days. The progressive pozzolanic consumption of CH facilitates the continuous precipitation of secondary, highly dense C-S-H gels, strictly refining the capillary network over time [21]. Although this ambient-strength deficit persists compared to pure cement matrices, the use of high-volume FA is justified by crucial functional trade-offs. As supported by existing literature, FA chemically mitigates thermal spalling by consuming the vulnerable CH phase, thereby providing superior fire resistance [39,40]. Furthermore, as detailed in the LCA evaluation, substituting 50% of the energy-intensive Portland cement delivers substantial environmental and economic benefits, drastically reducing the overall carbon footprint of the construction element [76,77].

To quantitatively correlate this microstructural evolution with macroscopic properties, the time-dependent relationship between compressive strength and acoustic velocity (UPV) was analyzed. As the curing period extended from 28 to 150 days, secondary hydration physically densified the internal pore structure and the interfacial transition zone (ITZ). For instance, the CFA50 mixture exhibited an outstanding 46.8% increase in compressive strength (from 38.50 to 56.50 MPa). This mechanical growth was directly accompanied by continuous acoustic densification, with UPV values rising progressively from 3980 m/s at 28 days to 4320 m/s at 150 days. Because ultrasonic waves travel significantly faster through a dense, solid medium than through air-filled voids, this 8.5% quantitative acoustic enhancement serves as a macroscopic physical indicator of the continuous micro-filler effect. The precipitation of secondary C-S-H gels systematically plugs the capillary voids. It strengthens the ITZ over 150 days, demonstrating that macroscopic strength development is a direct consequence of this prolonged microscopic densification.

Conversely, incorporating 1% volumetric SF independently led to distinct microstructural behavior at ambient temperatures, reducing the 28-day compressive strength by 11.1% (to 55.38 MPa) compared to the unreinforced matrix. The rigid, high-aspect-ratio geometry of steel SF inherently restrains fresh paste mobility, obstructing ideal compaction. The non-homogeneous distribution of these fibers entraps excessive air, inflating the initial void volume within the interfacial transition zones (ITZ) [52]. Under uniaxial compression at 20 °C, these entrapped interfacial voids act as stress concentrators. Nevertheless, as the hydration progressed and the binding matrix densified towards 150 days, this void-induced structural deficit was effectively neutralized, minimizing the disparity between the CF and control mix to a negligible 4.4%.

3.2. Effect of Elevated Temperatures (300 °C and 600 °C) on Mechanical Properties

The residual compressive strength kinetics of the mixtures exposed to extreme thermal loads are presented in Figure 5. To precisely quantify the degradation mechanisms, the residual strength ratio (R) was evaluated as the quotient of the high-temperature capacity and the corresponding ambient reference capacity.

As thermal exposure increased to 300 °C, the dominant degradation mechanism shifted to hydrothermal damage. At this intermediate temperature threshold, the free

water residing within the capillary network and a portion of the chemically bound gel water vaporize rapidly, exerting intense internal vapor pressures. Once this vapor pressure surpasses the inherent tensile limits of the binding matrix, destructive micro-crack networks are initiated [22]. The control mixture (C) showed a continuous decline in load-bearing capacity, yielding an R value of 0.698 at 28 days, which dropped to 0.629 at 150 days. This counterintuitive age-dependent strength loss occurs because the highly densified, impermeable late-age cementitious matrix severely obstructs vapor dissipation, trapping the expanding gas and inducing massive internal bursting stresses [78]. However, the inclusion of steel SF strictly neutralized these vapor-induced tensile stresses. The CF mixture preserved a remarkable residual ratio of 0.849 at 150 days, as the rigid metallic inclusions mechanically bridged the expanding vapor cracks and prevented structural separation.

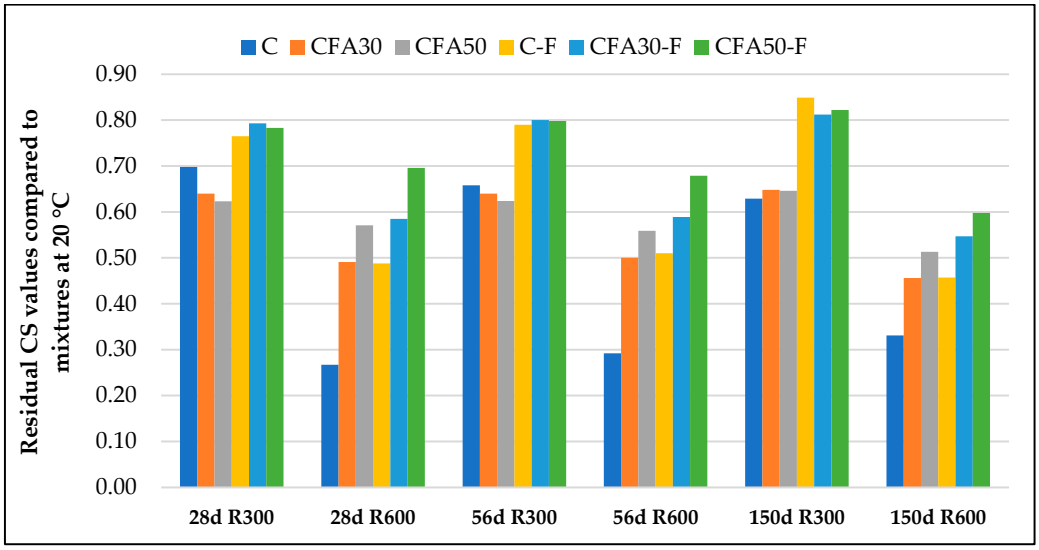
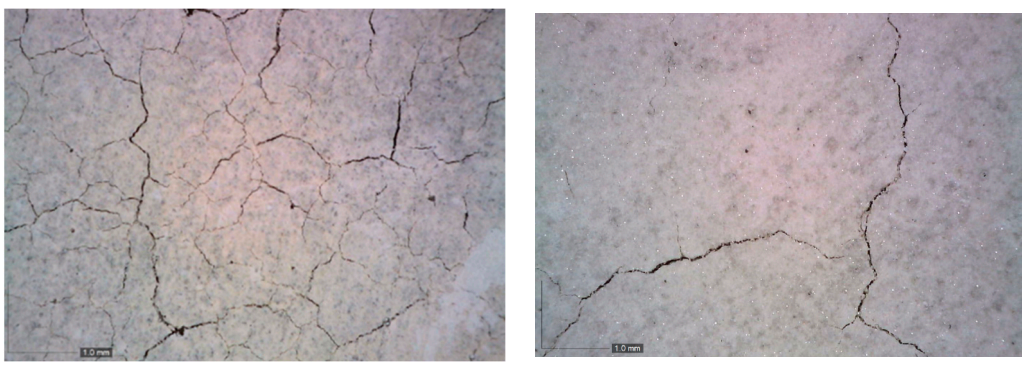


Figure 5. Residual compressive strength performance.

Heating the composites to 600 °C, the extreme limit, triggered severe thermochemical decomposition, compounding the physical damage. At temperatures exceeding 400 °C, the portlandite (CH) phase rapidly dehydrates into highly reactive calcium oxide (CaO), and the primary C-S-H gels lose their amorphous binding nature [18,19]. This synchronized chemical breakdown led to a catastrophic collapse of the unreinforced matrix. The 150-day compressive strength of the C series plummeted to 23.12 MPa, yielding a critically low R-value of 0.331. The severe macro-cracking manifested on the surface of the unreinforced control specimens at 600 °C is visually confirmed in Figure 6a.



(**a**) (**b**)

Figure 6. Cracks on the surface of specimens exposed to 600 °C temperature: (**a**) Control mixture, (**b**) Steel fibrous mixture.

In sharp contrast, high-volume FA substitution provided a distinct chemical shield against this degradation. The CFA50 mixture retained 51.3% of its initial capacity (R = 0.513) at 150 days. By aggressively consuming CH during ambient pozzolanic reactions, FA severely restricts the total volume of CH available to decompose into expansive CaO at 600 °C, proactively preventing expansion-induced internal ruptures [67].

The optimal thermal-shock endurance was observed in the hybrid CFA50-F mixture. At 600 °C, this composite achieved an exceptional R value of 0.696 at 28 days. Although this ratio is slightly adjusted to 0.598 at 150 days due to the heavily densified late-age matrix restricting vapor release, preserving nearly 60% of its extreme late-age strength at 600 °C proves the existence of a vital two-tier defense. The fine FA particles secure chemical stability against CaO expansion, while the SF mechanically locks the matrix against severe volumetric deformations, effectively restricting macro-crack formation (Figure 6b).

The comparative visual assessment of macroscopic surface damage in plain and FA-modified specimens is shown in Figure 7.

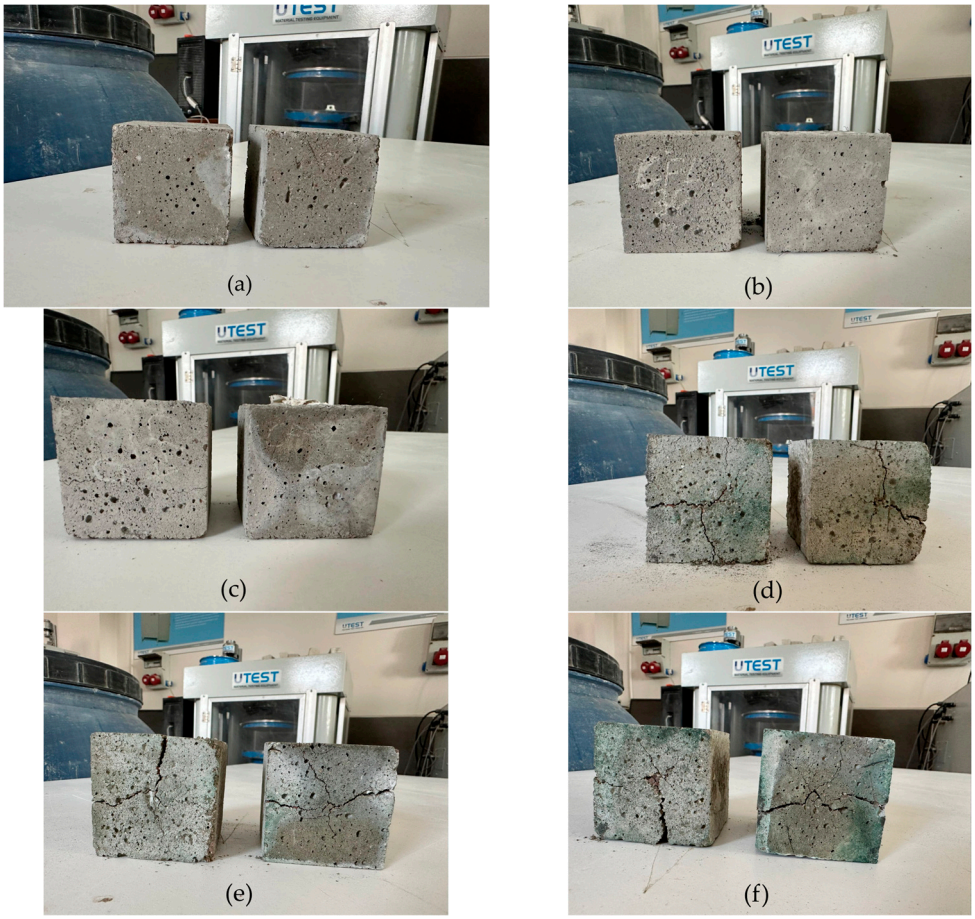


Figure 7. Comparative visual assessment of macroscopic surface damage in plain and FA and/or fiber-modified specimens after thermal exposure (In the figure, samples on the left are not reinforced with fiber and samples on the right are reinforced with fiber) (**a**) C-300 °C, (**b**) CFA30-300 °C, (**c**) CFA50-300 °C, (**d**) C-600 °C, (**e**) CFA30-600 °C, and (**f**) CFA50-600 °C.

The macroscopic degradation and characteristic color changes on the specimen surfaces directly confirm these thermochemical transformations and the protective role of fly ash. As shown in Figure 7, after exposure to 300 °C, the specimens exhibited a pale, yellowish hue resulting from the near-complete evaporation of physically unbound water and the onset of early hydration product decomposition [17,22]. At this intermediate stage (Figure 7a–c), both plain and FA-modified specimens maintained their general volumetric

shape. However, initial micro-cracking due to internal vapor pressure became visible on the surfaces.

Upon reaching 600 °C, severe structural deterioration and deeper grayish/reddish color tones became evident across the matrices (Figure 7d–f). In conventional Portland cement mixtures (C-600 °C), this severe macro-cracking is primarily driven by the dehydration of calcium hydroxide (Ca $(OH)_2$) into calcium oxide (CaO) and water [17,18]. During the cooling phase, the highly reactive CaO absorbs atmospheric moisture and carbon dioxide, reverting to $Ca(OH)_2$ and $CaCO_3$. This reversible chemical reaction triggers massive, localized volume expansions, generating intense internal bursting stress [19,20]. Furthermore, as the temperature rises to 600 °C, the thermal expansion and surface deformation of the steel fibers themselves negatively affect the surrounding matrix. In a plain cement paste, these opposing thermal movements heavily degrade the already weakened ITZ, leading to premature fiber debonding and severe surface spalling (Figure 7d) [76].

However, the visual evidence strongly supports the chemical shielding effect of high-volume fly ash. In the CFA30 and CFA50 matrices exposed to 600 °C (Figure 7e,f), the surface crack widths are visibly narrower, and the overall matrix integrity is significantly better preserved compared to the control group. By aggressively consuming CH during the prolonged 150-day ambient pozzolanic reactions, FA severely restricts the total volume of CH available to decompose into expansive CaO [67]. This chemical mitigation prevents the development of massive internal expansion stresses, preserving a dense, uncorrupted ITZ around the steel fibers. This intact anchorage zone enables the fibers to effectively bridge the thermal macro-cracks rather than pulling out, visually and mechanically validating the exceptional synergistic thermo-mechanical resilience of the CFA50-F hybrid composite.

The deterioration of flexural capacity, which is extremely sensitive to internal micro-crack propagation, is depicted in Figure 8.

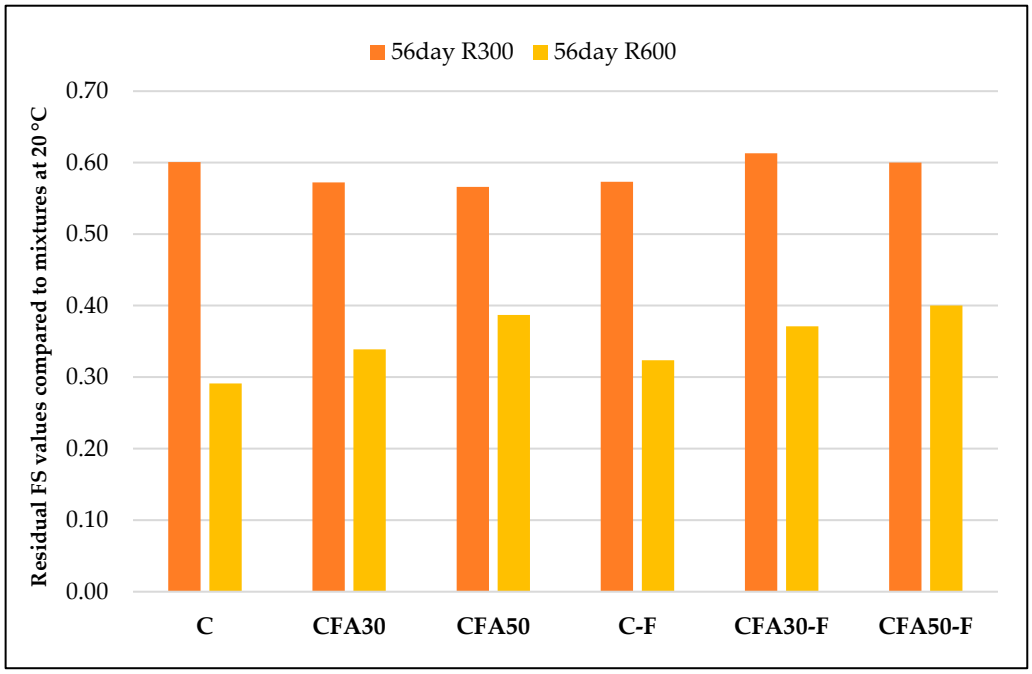


Figure 8. Residual flexural strength performance.

The flexural performance degradation exhibited a closely corresponding destructive trend. At 300 °C, the 56-day R values of all specimen groups clustered tightly within a narrow 0.57–0.61 band. At this stage, the localized tensile stresses generated by the escaping steam initiate internal micro-cracks. Under bending loads, these cracks propagate

instantly, causing uniform, unavoidable flexural performance drops across both plain and reinforced matrices [79].

Exposure to 600 °C radically amplified structural brittleness. The unreinforced C mixture exhibited the greatest degradation, retaining only 29% (R = 0.29) of its ambient flexural capacity due to the complete thermochemical breakdown of the primary tensile-bearing hydrates. The standalone inclusion of SF (CF) yielded a modest improvement, raising the R value to only 0.32. At extreme temperatures, the decomposition and thermal expansion of pure cement paste drastically weaken the fiber-matrix ITZ. Consequently, the degraded paste fails to provide a solid anchorage, triggering premature fiber pull-out under bending loads rather than an effective crack-bridging action [79].

Conversely, the CFA50 mixture sustained a superior R value of 0.39 at 600 °C, as the chemical depletion of CH preserved the microstructural continuity of the tension zone. Ultimately, the synergistic CFA50-F combination achieved the peak flexural residual ratio of 0.40. In this hybrid mechanism, FA chemically restricts severe CaO expansions and maintains a solid, intact anchorage environment for the SF. These securely anchored fibers then provide optimal bridging across thermally induced microcracks, significantly delaying brittle failure under high-temperature bending [52].

3.3. Thermal Damage: The Hybrid Use of Steel Fiber and Fly Ash

To precisely isolate the protective efficiency of the admixtures under extreme thermal shock, the absolute capacities of the mixtures at 600 °C were normalized against the unreinforced control mixture (Control 600 °C = 100%). The relative compressive and flexural evaluations are presented in Figures 9 and 10.

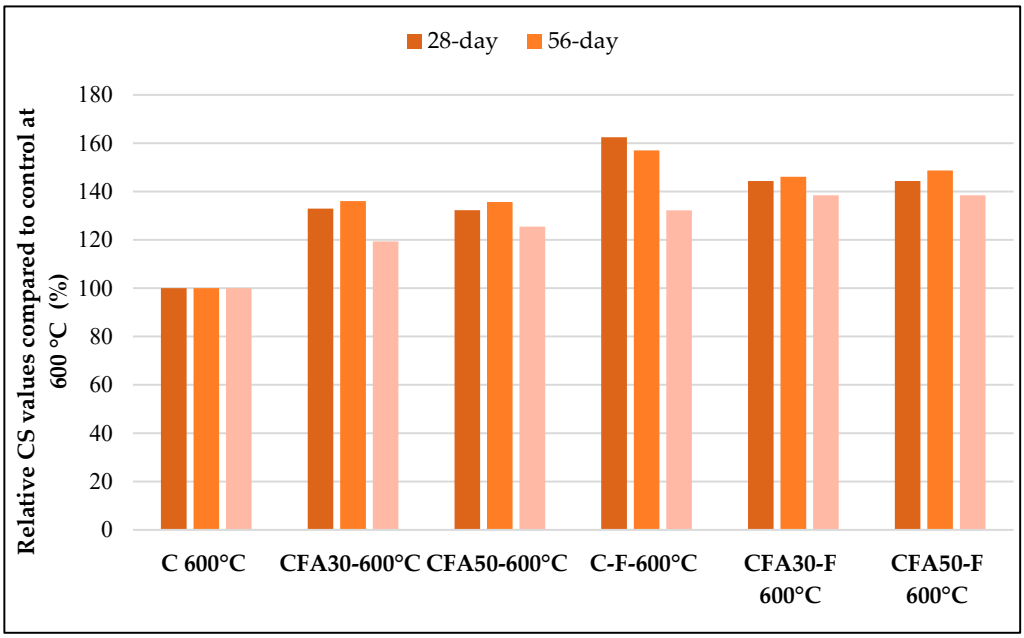


Figure 9. Relative CS values compared to the control at 600 °C.

Evaluating the standalone incorporation of SF reveals a massive relative advantage at early curing ages, achieving 162.42% and 156.96% of the control's compressive capacity at 28 and 56 days, respectively. As the decomposed CaO rehydrates and forces the matrix to expand during the cooling phase, the high-melting-point SF effectively absorbs the localized tensile stresses across the separating crack planes, preventing explosive spalling [47]. However, at 150 days of age, this relative superiority plummeted to 132.18%. In a highly matured, pure Portland cement paste containing zero FA, the matrix undergoes total thermochemical decomposition at 600 °C. This extensive microstructural destruction

thoroughly softens the ITZ, forcing the fibers to pull out prematurely under axial loading before they can fully utilize their tensile bridging capacity [79].

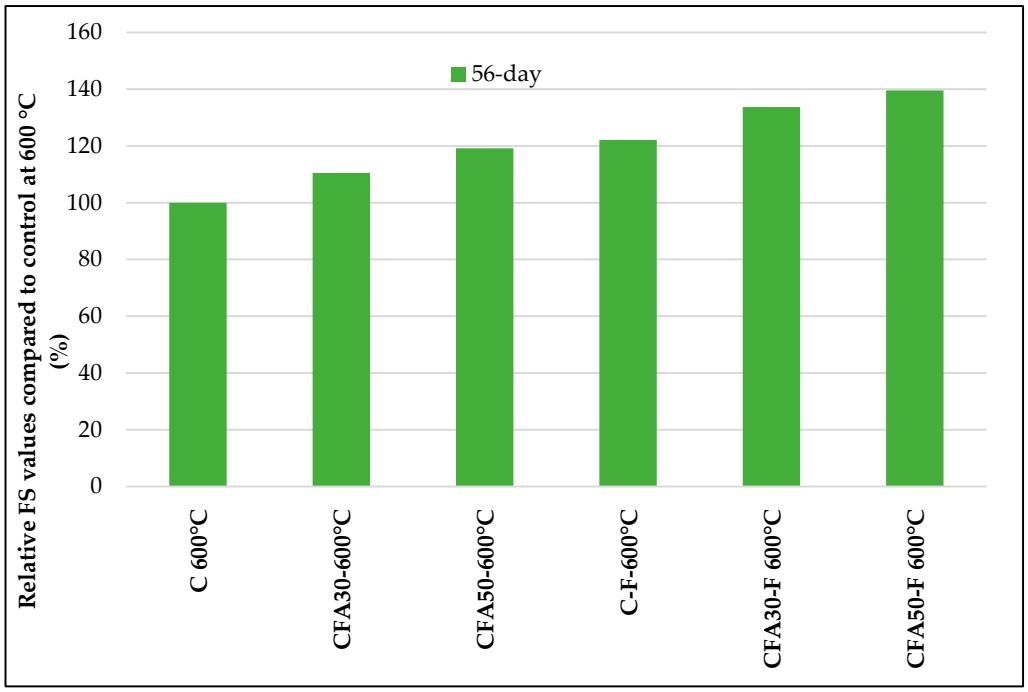


Figure 10. Relative FS values compared to the control at 600 °C.

High-volume FA substitution provided a highly consistent, chemistry-driven shield. The standalone FA matrices systematically outperformed the control group, maintaining a robust 125.43% relative capacity at 150 days (for CFA50). By continuously consuming CH during the 150-day ambient hydration, FA severely limits the internal CaO expansion stresses triggered at 600 °C, flawlessly preserving matrix integrity [21].

The 150-day relative performance data most clearly demonstrate the absolute necessity of the FA-SF synergy. Although the hybrid CFA50-F mixture initially underperformed the purely fibrous CF mixture at 28 days (144.32%), its late-age thermal endurance proved overwhelmingly superior. At 150 days, both hybrid systems (CFA30-F and CFA50-F) recorded the maximum relative compressive capacity of 138.41%. The ultra-fine FA particles chemically stabilize the matrix against internal expansion, sustaining an intact and firm micro-environment directly around the metallic inclusions. This uncorrupted matrix provides the robust anchorage zone necessary to prevent fiber pull-out. The securely anchored fibers then fully restrict crack propagation, proving that the chemical stabilization provided by FA is an indispensable prerequisite for unlocking the physical bridging potential of SF at late ages.

Normalizing the 56-day flexural performance at 600 °C isolates the tensile-protective capabilities. The standalone CFA50 mixture achieved a relative flexural strength of 119.19%, as chemical mitigation with CaO prevented early disintegration of the tension zone. The purely fibrous CF mix recorded 122.09%, heavily limited by the previously discussed high-temperature pull-out mechanism caused by the decomposing pure cement paste.

The hybrid CFA50-F mixture delivered an extraordinary relative flexural endurance of 139.53%. This peak performance validates a sequential, two-step protection mechanism. Initially, the micro-filler effect and pozzolanic activity of FA chemically stabilize the matrix and physically densify the ITZ, locking the SF firmly in place even after 600 °C exposure. Subsequently, acting from these robust anchorage points, the SF successfully bridges the

macro-cracks induced by extreme bending, generating a highly ductile composite capable of absorbing massive thermal deformations without breaking [40].

The hybrid CFA50-F mixture delivered an extraordinary relative flexural endurance of 139.53%. This peak performance validates a sequential, two-step protection mechanism driven by profound microstructural modifications at the fiber-matrix boundary. In a conventional Portland cement matrix, the Interfacial Transition Zone (ITZ) surrounding the rigid steel fibers is characteristically porous and highly enriched with large, oriented calcium hydroxide (CH) crystals, creating a distinct weak link [58]. Incorporating high-volume FA fundamentally heals this vulnerability through both physical and chemical pathways. Physically, the unreacted spherical FA particles exert a strong "micro-aggregate effect", efficiently packing into the interstitial voids around the brass-coated steel fibers and reducing initial boundary porosity. Chemically, the prolonged pozzolanic reactions specifically target and consume the oriented CH crystals accumulated at the ITZ, precipitating dense, amorphous secondary C-S-H gels directly onto the fiber surface [79,80].

This microstructural densification becomes critically decisive at 600 °C. By eliminating the CH phase at the fiber interface, FA prevents the disruptive volume expansion of CaO directly at the anchorage zone during cooling. Preserving the structural integrity of this boundary layer sustains the vital frictional bond and mechanical interlock between the metallic fiber and the cementitious matrix [81]. Consequently, rather than suffering from the premature pull-out observed in pure cement matrices, the firmly anchored steel fibers in the CFA50-F composite successfully bridge the macro-cracks induced by extreme bending, generating a highly ductile composite capable of absorbing massive thermal deformations without catastrophic failure [40].

3.4. Non-Destructive Test (UPV) and Structural Integrity

UPV serves as an extremely precise non-destructive diagnostic tool for monitoring internal void expansion and thermal micro-crack propagation. The progressive UPV loss ratios, calculated relative to the 20 °C reference conditions, are detailed in Figure 11.

Following 300 °C exposure (Figure 11a), the unreinforced control mixture (C) exhibited an age-dependent escalation in acoustic attenuation, widening its UPV loss from 13.70% at 28 days to 18.70% at 150 days. This severe late-age acoustic drop verifies that the highly compacted 150-day cementitious matrix restricts the escape of internal steam. The trapped vapor exerts internal hydraulic pressures, fracturing the matrix and generating new micro-crack networks that severely scatter the ultrasonic waves [22]. High-volume FA substitution perfectly inverted this destructive mechanism. The UPV loss of the CFA50 mixture diminished drastically from 13.30% at 28 days to a negligible 7.40% at 150 days. The delayed precipitation of secondary C-S-H gels creates a much higher thermal threshold, enabling it to successfully resist intermediate hydrothermal damage without forming wave-scattering voids.

Upon exposure to the extreme 600 °C threshold (Figure 11b), massive acoustic attenuation was observed across all mixtures. The unreinforced control matrix lost 50.80% of its acoustic velocity at 150 days. This catastrophic drop is physical proof of extensive, interconnected crack networks resulting from thermochemical dehydration, acting as absolute acoustic barriers that radically extend pulse travel times [47].

Consistent with the mechanical findings, the hybrid CFA50-F formulation limited its UPV loss to 41.40% at 150 days. The FA particles chemically neutralized the CaO expansion, preserving a reasonably continuous solid medium. Simultaneously, the SF physically held the fracture planes together.

To visualize this acoustic continuity at 600 °C independently of ambient variations, the absolute UPV values were normalized relative to the control mixture (Figure 12).

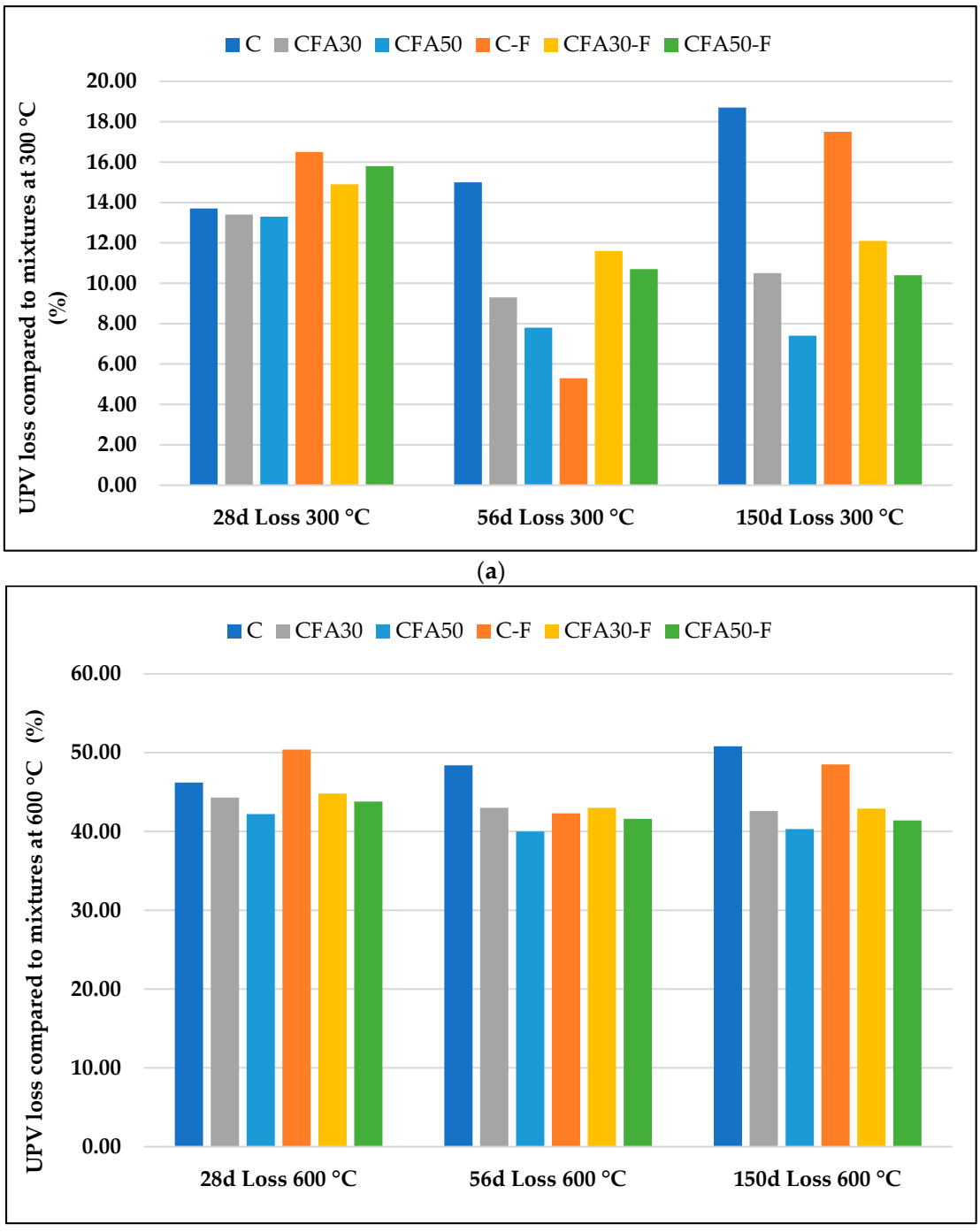


Figure 11. UPV loss performance: (**a**) exposed to 300 °C, (**b**) exposed to 600 °C.

The purely fibrous CF mixture provided negligible relative acoustic improvement under extreme heat (102.47% at 150 days). In the absence of FA, the high-temperature decomposition of the cement paste causes total debonding at the fiber-matrix ITZ. These debonded metallic interfaces merely act as additional wave-scattering barriers, entirely nullifying the acoustic conductivity of the steel [23]. Conversely, the hybrid CFA50-F mixture achieved the peak relative acoustic velocity of 119.05%. By chemically securing the ITZ against degradation, FA ensures that the steel SF remains tightly bonded. Instead of scattering at separated interfaces, the ultrasonic pulses utilize these securely anchored metallic inclusions as rapid "acoustic highways" to bypass the mechanically bridged micro-cracks [67].

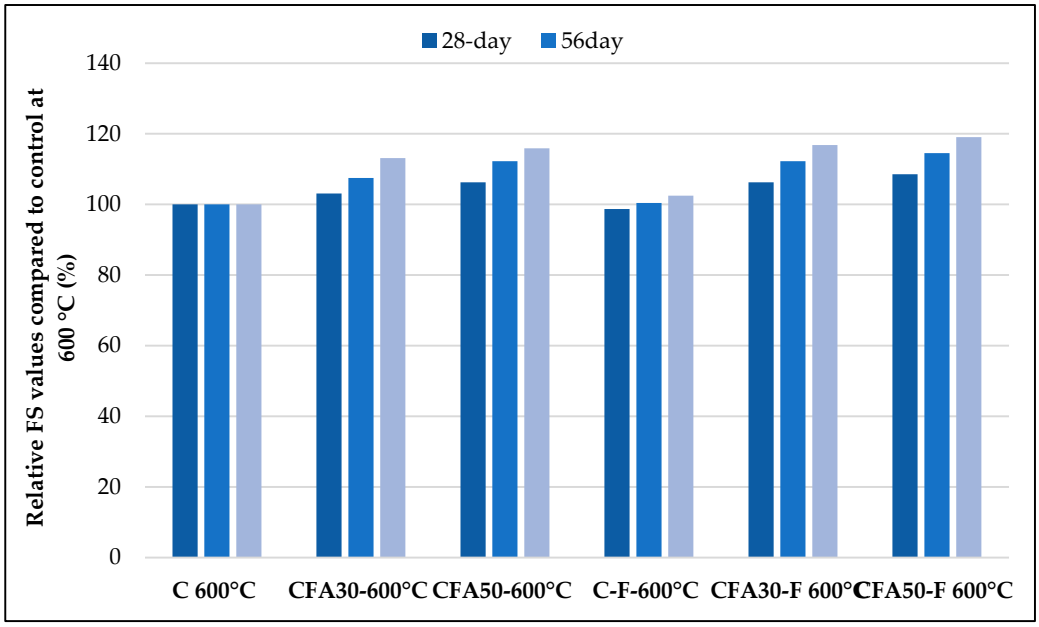


Figure 12. Relative UPV values compared to the control at 600 °C.

3.5. Physical Degradation: Water Absorption and Porosity Evolution

The physical degradation and structural permeability of the composites were evaluated through water absorption (WA) tests. To independently track the evolution of thermal damage, the high-temperature WA metrics were assessed by absolute increases (Figure 13) and by normalizing capacities relative to the unreinforced control mixture (Figure 14).

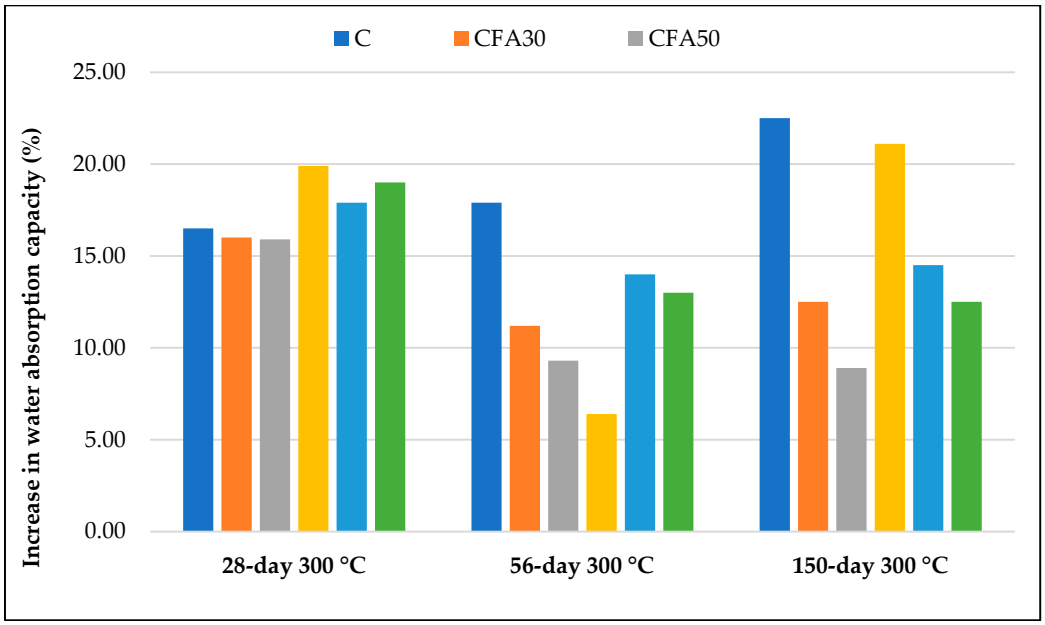
At 300 °C (Figure 13a), the control mixture exhibited an age-dependent expansion in its capillary network, with its absolute WA increase surging from 16.50% at 28 days to 22.50% at 150 days. In parallel with the UPV loss findings, the entrapment of vapor pressure inside the dense 150-day matrix forced the capillary walls to split, raising the macroscopic permeability [78]. High-volume FA reversed this degradation completely; the WA increase in the CFA50 mixture systematically declined from 15.90% to 8.90% at 150 days, as the thermally stable secondary C-S-H gels refined the pore structure and resisted internal steam ruptures. The singular use of SF (CF) triggered high WA increases (21.10% at 150 days) because the rigid fibers restrict fresh paste flow, intrinsically trapping large pockets of initial air within the ITZ [52].

Following extreme exposure at 600 °C (Figure 13b), the thermochemical dehydration of C-S-H gels and thermal incompatibilities between aggregate paste caused a dramatic surge in permeability. The WA increase in the unreinforced C mix reached a highly porous 61.00% at 150 days.

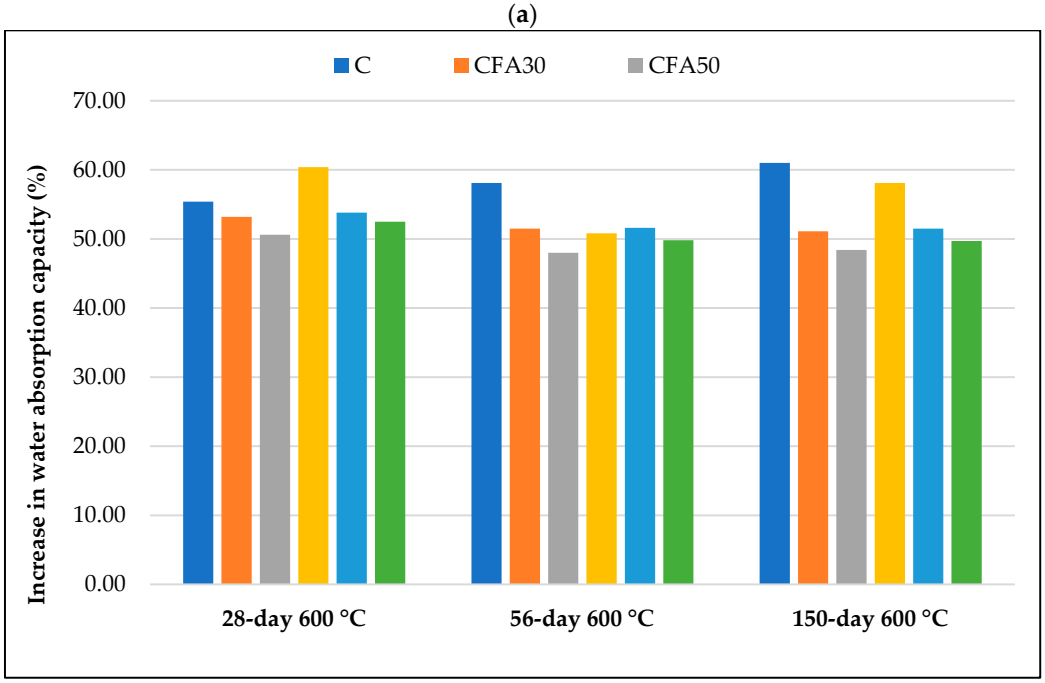
In the relative assessment (Figure 14), where values below 100% denote a denser microstructure than the control, the standalone CF mixture remained critically vulnerable, recording 103.05% at 150 days. At 600 °C, the initial ITZ voids generated by the fibers interconnect freely with the newly formed thermal microcracks, creating massive moisture-infiltration pathways.

However, the CFA50-F hybrid mixture successfully restricted its absolute WA increase to just 49.70% (Figure 13b) and delivered a remarkable relative absorption of 89.92% at 150 days (Figure 14). Although the hybrid mixture initially suffered high porosity at 28 days due to fiber-induced air entrapment and slow pozzolanic reactions (101.19% relative WA), the 150-day results confirm a profound progressive physical healing mechanism. The ultra-fine spherical morphology of the maturing FA particles functions as an exceptional micro-filler, perfectly plugging the excess ITZ voids generated by the SF [21]. Ultimately,

while the SF supplies essential mechanical bridging against macro-expansion, the high-volume FA simultaneously seals the micro-porosity, finalizing an optimally impermeable and mechanically robust composite against extreme thermal shocks.



(**a**)



(**b**)

Figure 13. Increase in water absorption ratios: (**a**) exposed to 300 °C, (**b**) exposed to 600 °C.

The macroscopic degradation of compressive and flexural strength under extreme thermal exposure is intrinsically governed by the evolution of internal damage, which is physically captured by the coupled non-destructive indicators: UPV and water absorption. A clear semi-quantitative and qualitative correlation exists among these three parameters. UPV loss primarily reflects the formation of internal wave-scattering acoustic barriers (closed and open macro-crack networks). At the same time, the increase in water absorption directly indicates the volumetric expansion and surface-breaking connectivity of these capillary pores. Together, they explain the exact physical mechanism behind the loss of

load-bearing capacity. For instance, at 600 °C, the unreinforced control mixture at 150 days exhibited a severe 50.8% UPV loss and a massive 61.0% increase in water absorption. This extreme physical degradation is perfectly correlated with its catastrophic 66.9% drop in compressive strength (from 69.92 to 23.12 MPa). The expanding CaO tears the matrix internally (blocking sound waves) and externally (allowing massive water ingress), leaving a highly porous structure completely unable to sustain mechanical stress. In sharp contrast, the CFA50-F mixture limited its UPV loss to 41.4% and the increase in water absorption to 49.7%. By simultaneously preserving acoustic continuity (crack bridging via fibers) and minimizing pore connectivity (void plugging via fly ash), the hybrid matrix retained a substantially higher load-bearing capacity. This strong correlation confirms that the degradation of mechanical properties in cementitious composites is directly proportional to the joint expansion of internal crack networks and to the interconnected porosity.

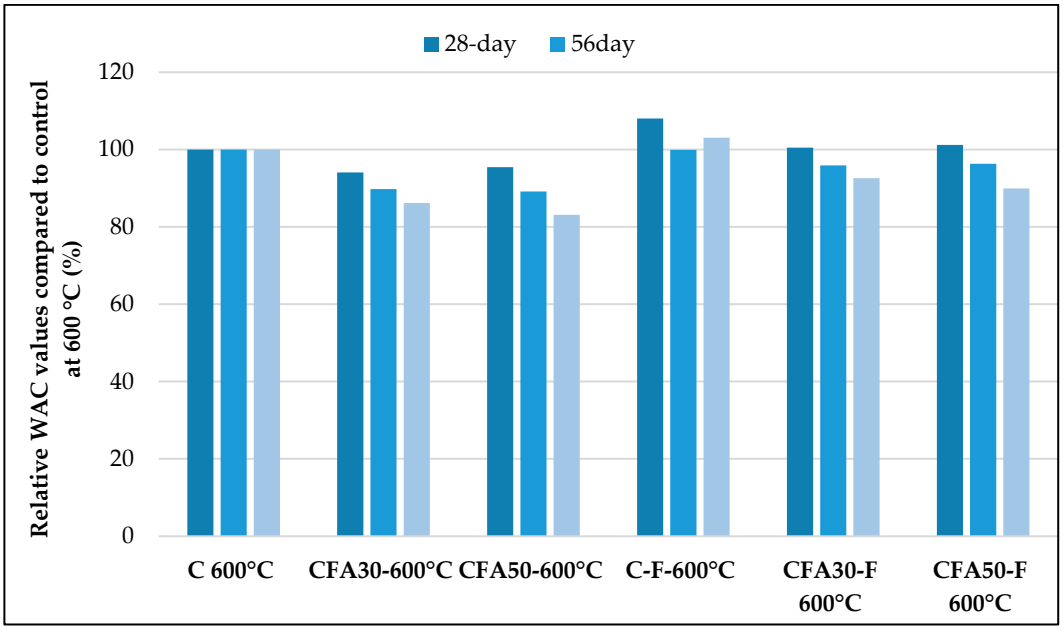


Figure 14. Relative WAC values compared to the control at 600 °C.

3.6. GWP and Service-Life Sustainability Assessment

To quantify the ecological viability of the proposed hybrid composites, a simplified "cradle-to-gate" Life Cycle Assessment (LCA) focusing on the Global Warming Potential (GWP) was conducted. The analysis utilized standard embodied carbon emission factors ($kgCO_2$-eq/kg) derived from established concrete sustainability literature: 0.86 for Portland cement, 0.02 for FA (allocated solely to processing and transport), 0.005 for aggregate, and 1.5 for the superplasticizer [82]. The emission factor for brass-coated SF was taken as 2.80 $kgCO_2$-eq/kg, reflecting the high energy intensity of steel wire manufacturing [76]. Based on the exact mixture proportions (Table 5), the absolute GWP was calculated per unit weight of the primary binder.

The initial static evaluation reveals a striking contrast in the environmental impact of the single-additive mixtures. The control mixture generated a baseline GWP of 0.880 $kgCO_2$-eq. The independent incorporation of 1% volumetric SF significantly increased total emissions to 1.279 $kgCO_2$-eq, representing a massive 45% carbon penalty at the production stage. In sharp contrast, substituting 50% of the cement with FA (CFA50) inherently collapsed the environmental burden. When these elements are combined in the hybrid CFA50-F mixture, the massive carbon deficit induced by the SF is entirely subsidized by the high-volume cement replacement. The absolute GWP of the CFA50-F mixture was

0.857 $kgCO_2$-eq, which is strictly lower than that of the unreinforced control, effectively nullifying the carbon penalty of the metallic reinforcement.

However, evaluating sustainability strictly at the production phase (absolute GWP) presents a scientifically flawed metric for durable cementitious composites. Traditional static LCA models that rely solely on production-stage material volumes heavily penalize fiber-reinforced structures while entirely ignoring their fundamental durability benefits and service-life extensions over time [77]. To provide a realistic environmental metric, an annualized service-life LCA (LCA_{annual}) was modeled and graphically presented in Figure 15.

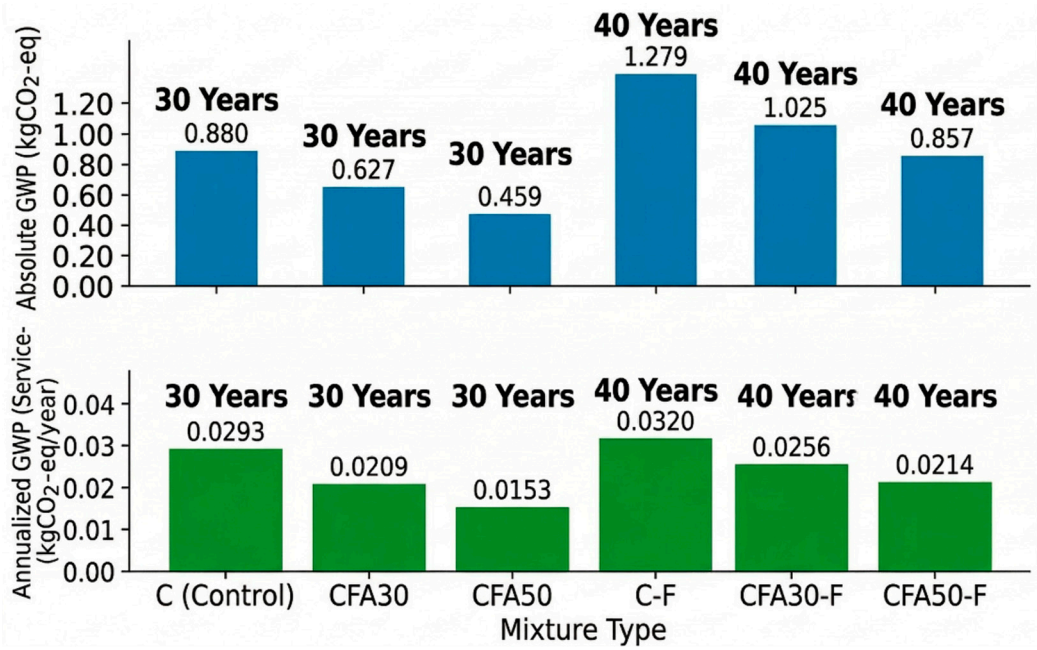


Figure 15. Sustainability assessment of all mixtures.

Under severe exposure conditions, such as thermal fatigue or industrial heat environments, unreinforced composites such as the C mixture suffer from unbridged macrocracking. As demonstrated by the catastrophic 61.0% increase in water absorption in the control group at 600 °C, this unbridged cracking creates massive ingress pathways for moisture and aggressive agents. This rapid physical degradation conservatively limits the safe structural service life of the plain matrix to an assumed 30 years. Conversely, the robust crack-bridging mechanism and microstructural stabilization provided by SF prevent catastrophic spalling and restrict progressive crack propagation. By tightly holding the fracture planes together, steel fibers significantly reduce post-cracking permeability and maintain the structural integrity of the element. As established in recent life-cycle and durability literature, the enhanced fracture toughness and damage tolerance provided by steel fibers in severe environments can extend the functional service life of the composite by over 30% compared to unreinforced concrete [77,83]. Based on this coupled experimental and literature-based evidence, an extended operational service life of 40 years was logically assigned to the fibrous matrices (C-F and CFA50-F), substantially diluting their long-term environmental footprint.

By distributing the total embodied carbon over the functional lifespan, the annualized carbon footprint isolates the hybrid design's ultimate sustainability. As depicted in Figure 15, the unreinforced control mixture yields an annual footprint of 0.0293 $kgCO_2$-eq/year. While the standalone CF mixture extends the service life to 40 years, its high absolute carbon content still yields an unfavorable annualized rate of 0.0320 $kgCO_2$-eq/year. True ecological optimization is realized in the CFA50-F matrix.

By synergizing the ultra-low embodied carbon of FA with the 40-year lifespan extension provided by SF, the CFA50-F mixture achieves an outstandingly low annual footprint of just 0.0214 $kgCO_2$-eq/year.

Consequently, replacing traditional concrete with the CFA50-F hybrid composite delivers a net 27% reduction in life-cycle environmental impact. This confirms that the synergistic use of high-volume FA and SF is not merely a mechanical necessity to prevent extreme thermal degradation, but a highly sustainable strategy that offers a superior "performance-to-carbon" ratio.

From a practical engineering perspective, the findings of this study can be directly implemented in several specific construction projects. The exceptional fire-resistance and spalling prevention provided by the CFA50-F composite make it highly suitable for underground infrastructure, particularly road and railway tunnels, where explosive spalling under confined fire events poses a catastrophic structural risk. Additionally, the superior thermal fatigue resistance and low annualized carbon footprint are ideal for heavy industrial facilities operating under continuous or cyclic high-temperature exposures, including metallurgical foundries, industrial chimneys, and cooling towers. Finally, in the commercial construction sector, utilizing this hybrid composite for the load-bearing cores and structural columns of high-rise buildings would simultaneously satisfy stringent fire-safety codes and modern green-building certification requirements (such as LEED or BREEAM) by drastically reducing the overall embodied carbon of the structural frame.

When contrasted with the broader literature, the scientific novelty and distinctiveness of this study become evident. The majority of existing research on fiber-reinforced cementitious composites under elevated temperatures is predominantly confined to early-age (28-day) mechanical evaluations and static, production-stage sustainability assessments [65,78]. In contrast, the originality of the current work lies in its multi-scale, long-term approach. By evaluating the extreme late-age (150-day) maturity of high-volume fly ash matrices, this study uniquely captures the delayed micro-filler effects and ITZ stabilization that are completely invisible in standard 28-day tests. Furthermore, while previously published works often treat physical degradation and environmental impact as isolated topics, this research successfully bridges them. By quantitatively correlating non-destructive acoustic damage (UPV) with an annualized service-life Life Cycle Assessment, this study moves beyond conventional short-term analyses, offering a profoundly original, life-cycle-oriented framework for designing thermo-mechanically resilient structures.

4. Conclusions

Based on experimental investigations, microstructural analyses, and annualized service-life LCA of high-volume fly ash- and steel fiber-reinforced composites exposed to extreme temperatures, the following clearly formulated conclusions are drawn:

- The independent use of steel fibers in pure Portland cement matrices fails at advanced curing ages under 600 °C exposure. For instance, the unreinforced 150-day control matrix suffered a catastrophic strength collapse down to 23.12 MPa, retaining only 33.1% of its ambient capacity. The thermochemical decomposition of the matrix and subsequent expansion of calcium oxide (CaO) destroys the interfacial transition zone (ITZ), leading to premature fiber pull-out rather than crack-bridging.
- Replacing 50% of the cement with fly ash fundamentally alters this degradation. Scientifically, it creates a two-step defense: First, the prolonged pozzolanic reactions chemically consume portlandite (preventing CaO expansion), while ultra-fine FA particles physically densify the ITZ. Second, this preserved, robust anchorage environment allows the steel fibers to remain firmly embedded and successfully bridge thermally induced macro-cracks.

- Driven by this hybrid synergy, the CFA50-F mixture delivers the highest residual compressive and flexural capacities, successfully retaining nearly 60% (32.00 MPa) of its extreme late-age strength at 600 °C. Furthermore, it successfully preserves internal acoustic continuity (restricting UPV loss to 41.4%) and severely restricts high-temperature capillary permeability (limiting the water absorption increase to 49.7%, compared to the massive 61.0% surge in the plain control matrix).
- Evaluating environmental impact based solely on static, production-stage carbon emissions inaccurately penalizes fiber-reinforced structures. Real-world sustainability metrics must account for structural service life.
- While steel fibers increase the initial global warming potential (GWP), substituting 50% of the clinker with FA completely subsidizes this carbon deficit. By preventing catastrophic spalling, the CFA50-F composite extends the operational lifespan of fire-exposed elements from 30 to 40 years, ultimately achieving a net 27% reduction in the annualized GWP.
- The developed hybrid composite delivers an optimal performance-to-carbon ratio. It is ready for direct implementation in high-risk construction projects, specifically for preventing explosive spalling in underground road/railway tunnels, resisting thermal fatigue in heavy industrial facilities, and constructing the load-bearing cores of green-certified high-rise buildings.
- While this study confirms the exceptional thermo-mechanical resilience of the CFA50-F hybrid composite, future research prospects should focus on evaluating the long-term durability of these thermally exposed matrices under aggressive chemical environments (e.g., chloride penetration or sulfate attack). Additionally, investigating the integration of multi-scale hybrid fiber systems could further optimize the cost-to-performance ratio of these sustainable composites.

Author Contributions: Methodology, K.K.; Investigation, K.K. and S.H.B.; Data curation, M.Ü., S.Ö. and K.K.; Writing—original draft, M.Ü., S.Ö., K.K. and S.H.B.; Writing—review & editing, A.M.; Supervision, A.M. All authors have read and agreed to the published version of the manuscript.

Funding: This research was funded by Bursa Uludağ University Science and Technology Center (BAP) grant numbers FGA-2025-2048 and FBG-2025-2550, and The APC was funded by BAP.

Data Availability Statement: Data are contained within the article.

Acknowledgments: The authors would like to thank the authorities of Bursa-Beton Ready Mixed Concrete Plant and Polisan Construction Chemicals Company for their kind assistance in providing the cement, fly ash, aggregate, and water-reducing admixture, as well as in determining the chemical composition and physical and mechanical properties of these materials. The authors express their gratitude for the project grant support from the Bursa Uludağ University Science and Technology Center (BAP), under project numbers FGA-2025-2048 and FBG-2025-2550.

Conflicts of Interest: The authors declare no conflict of interest.

References

1. Boulebnane, M.A.; Belkadi, A.A.; Chiker, T. Impact of Aggregate Properties on the Microstructural Performance of Concrete Exposed to High Temperatures: An Analytical Review. *Int. J. Adv. Nat. Sci. Eng. Res.* **2023**, *7*, 243–250. [CrossRef]
2. Wan, X.; Tan, Y.; Long, X. Effects of Incorporating Steel Fibers and Municipal Waste on the Compressive Strength of Concrete. *SDHM Struct. Durab. Health Monit.* **2024**, *18*, 505–524. [CrossRef]
3. Abdulkareem, O.A.; Mustafa Al Bakri, A.M.; Kamarudin, H.; Khairul Nizar, I.; Saif, A.A. Effects of Elevated Temperatures on the Thermal Behavior and Mechanical Performance of Fly Ash Geopolymer Paste, Mortar and Lightweight Concrete. *Constr. Build. Mater.* **2014**, *50*, 377–387. [CrossRef]
4. Çavdar, A. A Study on the Effects of High Temperature on Mechanical Properties of Fiber Reinforced Cementitious Composites. *Compos. B Eng.* **2012**, *43*, 2452–2463. [CrossRef]

5. Türkmen, I.; Kantarci, A. Effects of Expanded Perlite Aggregate and Different Curing Conditions on the Physical and Mechanical Properties of Self-Compacting Concrete. *Build. Environ.* **2007**, *42*, 2378–2383. [CrossRef]
6. Zhang, D.; Tan, G.Y.; Tan, K.H. Combined Effect of Flax Fibers and Steel Fibers on Spalling Resistance of Ultra-High Performance Concrete at High Temperature. *Cem. Concr. Compos.* **2021**, *121*, 104067. [CrossRef]
7. Wen, Y.; Wang, Z.; Yuan, X.; Yang, X. Optimization of Mechanical Properties and Durability of Steel Fiber-Reinforced Concrete by Nano CaCO3 and Nano TiC to Improve Material Sustainability. *Sustainability* **2025**, *17*, 641. [CrossRef]
8. Macmac, J.D.; Clemente, S.J.C.; Ongpeng, J.M.C. Corrosion Resistance Analysis of Tire Waste Steel Fiber Reinforced Self-Compacting Concrete Using Rapid Chloride Penetration Test. *Chem. Eng. Trans.* **2024**, *114*, 463–468. [CrossRef]
9. Yu, J.; Abdalla, J.A.; Hawileh, R.A.; Zhang, X.; Zhang, Z. Corrosion Inhibition in Concrete: Synergistic Performance of Hybrid Steel-Polypropylene Fiber Reinforcement Against Marine Salt Spray. *Polymers* **2025**, *17*, 2645. [CrossRef] [PubMed]
10. Zhu, P.; Zhou, X.; Liu, X.; Liang, N.; Wang, L.; Li, L. Corrosion Resistance Mechanism of Concrete Containing Modified Fly Ash and Modified Zeolite Powder in a Wet–Dry Cyclic Sulfate Environment. *J. Mater. Civ. Eng.* **2025**, *37*, 04025270. [CrossRef]
11. Ahmed, M.F. Enhancing the External Sulfate Attack Resistance of High-Volume Fly Ash Concrete Containing Waste Glass Powder. *Res. Eng. Struct. Mater.* **2025**, *12*, 971–979. [CrossRef]
12. İsafça-Kaya, T.; Kaya, Y.; Mardani, N.; Mardani, A.; Doğangün, A. Improving Lime-Based Restoration Mortars: Effect of Type and Utilization Rate of Binder and Aggregate. *Materials* **2025**, *18*, 961. [CrossRef]
13. Tao, Y.; Zhang, Y.; Zhao, C.; Bu, C.; Zhang, R.; Wang, Q.; Yi, Q.; Wu, F.; Zhu, Y.; Fang, Y. Freeze–Thaw Durability and Damage Evolution of High-Strength Concrete Reinforced with Steel–Polypropylene Hybrid Fibers. *Fibers* **2026**, *14*, 28. [CrossRef]
14. Chen, Q.; Wang, A.; Duan, J.; Jin, W.; Shi, B.; Huang, M.; Chen, D. Fracture Damage and Softening Constitutive Relationship of Polyethylene Fiber-Reinforced Composite Concrete under Freeze–Thaw Cycles. *Can. J. Civ. Eng.* **2025**, *52*, 1180–1192. [CrossRef]
15. Wu, L.M.; Gao, F.; Huang, H.X.T.; Luo, W.J.; Liu, G.N. An Experimental Investigation of Constitutive Models for Steel Fiber-Reinforced Concrete Tunnel Linings Subjected to Freeze–Thaw Cycles. *Buildings* **2026**, *16*, 957. [CrossRef]
16. Valipour, M.; Pargar, F.; Shekarchi, M.; Khani, S. Comparing a Natural Pozzolan, Zeolite, to Metakaolin and Silica Fume in Terms of Their Effect on the Durability Characteristics of Concrete: A Laboratory Study. *Constr. Build. Mater.* **2013**, *41*, 879–888. [CrossRef]
17. Gao, D.; Zhao, L.; Chen, G. Flexural Behavior of Fiber and Nanoparticle Reinforced Concrete at High Temperatures. *Fire Mater.* **2018**, *42*, 725–740. [CrossRef]
18. Kuranlı, Ö.F.; Uysal, M.; Abbas, M.T.; Cosgun, T.; Niş, A.; Aygörmez, Y.; Canpolat, O.; Al-mashhadani, M.M. Evaluation of Slag/Fly Ash Based Geopolymer Concrete with Steel, Polypropylene and Polyamide Fibers. *Constr. Build. Mater.* **2022**, *325*, 126747. [CrossRef]
19. Doğruyol, M.; Ayhan, E.; Karaşin, A. Effect of Waste Steel Fiber Use on Concrete Behavior at High Temperature. *Case Stud. Constr. Mater.* **2024**, *20*, e03051. [CrossRef]
20. Celik, A.; Yilmaz, K.; Canpolat, O.; Al-mashhadani, M.M.; Aygörmez, Y.; Uysal, M. High-Temperature Behavior and Mechanical Characteristics of Boron Waste Additive Metakaolin Based Geopolymer Composites Reinforced with Synthetic Fibers. *Constr. Build. Mater.* **2018**, *187*, 1190–1203. [CrossRef]
21. Yıldırım, M.; Özhan, H.B. Durability Properties of Basalt Fiber-Reinforced Mortars with Different Mineral Admixtures Exposed to High Temperatures. *Constr. Build. Mater.* **2023**, *400*, 132574. [CrossRef]
22. Durgun, M.Y.; Özen, S.; Karakuzu, K.; Kobya, V.; Bayqra, S.H.; Mardani-Aghabaglou, A. Effect of High Temperature on Polypropylene Fiber-Reinforced Mortars Containing Colemanite Wastes. *Constr. Build. Mater.* **2022**, *316*, 125827. [CrossRef]
23. Raif Boğa, A.; Karakurt, C.; Ferdi Şenol, A. The Effect of Elevated Temperature on the Properties of SCC's Produced with Different Types of Fibers. *Constr. Build. Mater.* **2022**, *340*, 127803. [CrossRef]
24. Atiş, C.D.; Görür, E.B.; Karahan, O.; Bilim, C.; Ilkentapar, S.; Luga, E. Very High Strength (120 MPa) Class F Fly Ash Geopolymer Mortar Activated at Different NaOH Amount, Heat Curing Temperature and Heat Curing Duration. *Constr. Build. Mater.* **2015**, *96*, 673–678. [CrossRef]
25. Karahan, O.; Atiş, C.D. The Durability Properties of Polypropylene Fiber Reinforced Fly Ash Concrete. *Mater. Des.* **2011**, *32*, 1044–1049. [CrossRef]
26. Kaur, M.; Singh, J.; Kaur, M. Microstructure and Strength Development of Fly Ash-Based Geopolymer Mortar: Role of Nano-Metakaolin. *Constr. Build. Mater.* **2018**, *190*, 672–679. [CrossRef]
27. Ouedraogo, H.A.; Özen, S.; Kobya, V.; Sagiroglu, S.; Mardani-Aghabaglou, A. Comparison of Fresh and Hardened Properties of Self-Compacting Concrete Mixture from Different Aspect Ratio of Steel Fiber View Point. *J. Green Build.* **2021**, *16*, 115–138. [CrossRef]
28. Unverdi, M.; Kazemi, R.; Kaya, Y.; Mardani, N.; Mardani, A.; Mirjalili, S. Predicting Compressive and Splitting Tensile Strength of High Volume Fly Ash Roller Compacted Concrete Using ANN and ANN-Biogeography Based Optimization Models. *Sci. Rep.* **2025**, *15*, 21794. [CrossRef]

29. Durak, U.; İlkentapar, S.; Karahan, O.; Uzal, B.; Atiş, C.D. A New Parameter Influencing the Reaction Kinetics and Properties of Fly Ash Based Geopolymers: A Pre-Rest Period before Heat Curing. *J. Build. Eng.* **2021**, *35*, 102023. [CrossRef]
30. Elyamany, H.E.; Abd Elmoaty, A.E.M.; Elshaboury, A.M. Magnesium Sulfate Resistance of Geopolymer Mortar. *Constr. Build. Mater.* **2018**, *184*, 111–127. [CrossRef]
31. Kaya, M.; Köksal, F. Influences of High Temperature on Mechanical Properties of Fly Ash Based Geopolymer Mortars Reinforced with PVA Fiber. *Rev. Constr.* **2021**, *20*, 393–406. [CrossRef]
32. Ling, Y.; Wang, K.; Li, W.; Shi, G.; Lu, P. Effect of Slag on the Mechanical Properties and Bond Strength of Fly Ash-Based Engineered Geopolymer Composites. *Compos. B Eng.* **2019**, *164*, 747–757. [CrossRef]
33. Faleschini, F.; Alejandro Fernández-Ruíz, M.; Zanini, M.A.; Brunelli, K.; Pellegrino, C.; Hernández-Montes, E. High Performance Concrete with Electric Arc Furnace Slag as Aggregate: Mechanical and Durability Properties. *Constr. Build. Mater.* **2015**, *101*, 113–121. [CrossRef]
34. Sarıdemir, M.; Çelikten, S. Investigation of Fire and Chemical Effects on the Properties of Alkali-Activated Lightweight Concretes Produced with Basaltic Pumice Aggregate. *Constr. Build. Mater.* **2020**, *260*, 119969. [CrossRef]
35. Topçu, I.B.; Boğa, A.R. Effect of Boron Waste on the Properties of Mortar and Concrete. *Waste Manag. Res.* **2010**, *28*, 626–633. [CrossRef] [PubMed]
36. Kaya, Y.; Kobya, V.; Eser, M.; Mardani, N.; Bilgin, M.; Mardani, A. Evaluation of the Effect of Using Different Types of Clinker Grinding Aids on Grinding Performance by Numerical Analysis. *Materials* **2025**, *18*, 2712. [CrossRef] [PubMed]
37. Beytekin, H.E.; Kaya, Y.; Mardani, A.; Sezer, F.Ş. Effect of Fiber Type, Size, and Utilization Rate on Mechanical and Thermal Properties of Lightweight Concrete Facade Panels. *Struct. Concr.* **2024**, *25*, 3824–3840. [CrossRef]
38. Yazici, Ş.; Ayekin, B.; Mardani-Aghabaglou, A.; Güller, C. Assessment of Mechanical Properties of Steel Fiber Reinforced Mortar Mixtures Containing Lightweight Aggregates Improved by Bacteria. *J. Sustain. Cem. Based. Mater.* **2023**, *12*, 97–115. [CrossRef]
39. Poon, C.S.; Azhar, S.; Anson, M.; Wong, Y.L. Comparison of the Strength and Durability Performance of Normal- and High-Strength Pozzolanic Concretes at Elevated Temperatures. *Cem. Concr. Res.* **2001**, *31*, 1291–1300. [CrossRef]
40. Cao, K.; Liu, G.; Li, H.; Huang, Z. Mechanical Properties and Microstructures of Steel-Basalt Hybrid Fibers Reinforced Cement-Based Composites Exposed to High Temperatures. *Constr. Build. Mater.* **2022**, *341*, 127730. [CrossRef]
41. Aydin, S.; Yazici, H.; Baradan, B. High Temperature Resistance of Normal Strength and Autoclaved High Strength Mortars Incorporated Polypropylene and Steel Fibers. *Constr. Build. Mater.* **2008**, *22*, 504–512. [CrossRef]
42. Aydin, A.C. Self Compactability of High Volume Hybrid Fiber Reinforced Concrete. *Constr. Build. Mater.* **2007**, *21*, 1149–1154. [CrossRef]
43. Mardani-Aghabaglou, A.; Yüksel, C.; Hosseinnezhad, H.; Ramyar, K. Performance of Steel Micro Fiber Reinforced Mortar Mixtures Containing Plain, Binary and Ternary Cementitious Systems. *J. Green Build.* **2016**, *11*, 109–130. [CrossRef]
44. Ding, Y.; Azevedo, C.; Aguiar, J.B.; Jalali, S. Study on Residual Behaviour and Flexural Toughness of Fibre Cocktail Reinforced Self Compacting High Performance Concrete after Exposure to High Temperature. *Constr. Build. Mater.* **2012**, *26*, 21–31. [CrossRef]
45. Biricik, Ö.; Bayqra, S.H.; Kaya, Y.; Mardani, A. Assessment of Mechanical Properties of Fiber Reinforced Cementitious System Exposed to High Temperature. *Struct. Concr.* **2023**, *24*, 4733–4750. [CrossRef]
46. Kaya, Y.; Biricik, Ö.; Bayqra, S.H.; Mardani, A. Effect of Fibre Type and Utilisation Rate on Dimensional Stability and Frost Resistance of Pavement Mortar Mixture. *Int. J. Pavement Eng.* **2023**, *24*, 2154351. [CrossRef]
47. Chen, Y.; Zhang, Y.; Zhang, S.; Guo, Q.; Gao, Y.; Zhang, T.; Zhao, W.; Chen, Q.; Zhu, H. Experimental Study on the Thermal Properties of a Novel Ultra-High Performance Concrete Reinforced with Multi-Scale Fibers at Elevated Temperatures. *Constr. Build. Mater.* **2023**, *366*, 130229. [CrossRef]
48. Mastali, M.; Dalvand, A. Use of Silica Fume and Recycled Steel Fibers in Self-Compacting Concrete (SCC). *Constr. Build. Mater.* **2016**, *125*, 196–209. [CrossRef]
49. Pająk, M.; Ponikiewski, T. Flexural Behavior of Self-Compacting Concrete Reinforced with Different Types of Steel Fibers. *Constr. Build. Mater.* **2013**, *47*, 397–408. [CrossRef]
50. Ünverdi, M.; Kaya, Y.; Mardani, N.; Mardani, A. Investigation of the Microstructural and Mechanical Properties of Fiber-Reinforced Roller-Compacted Concrete Under High-Temperature Exposure. *Materials* **2025**, *18*, 2430. [CrossRef]
51. Oguz, M.; Özen, S.; Yazıcı, Ş.; Mardani, A. Influence of Steel and Polypropylene Fibers on Flexural Strength and Fracture Properties of Ambient-Cured Geopolymer Concrete. *Polymers* **2026**, *18*, 873. [CrossRef] [PubMed]
52. Funda Akbulut, Z.; Guler, S.; Khan, M. The Effects of Waste Iron Powder and Steel Fiber on the Physical and Mechanical Properties of Geopolymer Mortars Exposed to High Temperatures. *Structures* **2023**, *58*, 105398. [CrossRef]
53. Aygörmez, Y.; Al-mashhadani, M.M.; Canpolat, O. High-Temperature Effects on White Cement-Based Slurry Infiltrated Fiber Concrete with Metakaolin and Fly Ash Additive. *Rev. Constr.* **2020**, *19*, 324–333. [CrossRef]
54. Banyhussan, Q.S.; Yıldırım, G.; Bayraktar, E.; Demirhan, S.; Şahmaran, M. Deflection-Hardening Hybrid Fiber Reinforced Concrete: The Effect of Aggregate Content. *Constr. Build. Mater.* **2016**, *125*, 41–52. [CrossRef]

55. Kumari, G.J.; Mousavi, S.S.; Bhojaraju, C. Influence of Thermal Cycles and High-Temperature Exposures on the Residual Strength of Hybrid Steel/Glass Fiber-Reinforced Self-Consolidating Concrete. *Structures* **2023**, *55*, 1532–1541. [CrossRef]
56. Li, L.; Gao, D.; Li, Z.; Cao, M.; Gao, J.; Zhang, Z. Effect of High Temperature on Morphologies of Fibers and Mechanical Properties of Multi-Scale Fiber Reinforced Cement-Based Composites. *Constr. Build. Mater.* **2020**, *261*, 120487. [CrossRef]
57. Afzal, M.T.; Khushnood, R.A. Influence of Carbon Nano Fibers (CNF) on the Performance of High Strength Concrete Exposed to Elevated Temperatures. *Constr. Build. Mater.* **2021**, *268*, 121108. [CrossRef]
58. Liu, F.; Ding, W.; Qiao, Y. Experimental Investigation on the Tensile Behavior of Hybrid Steel-PVA Fiber Reinforced Concrete Containing Fly Ash and Slag Powder. *Constr. Build. Mater.* **2020**, *241*, 118000. [CrossRef]
59. Krishna, A.; Sreekumaran, S.; Kaliyaperumal, S.R.M.; Dixit, S.; Shahare, P.; Bansal, S.; Memoria, M.; Krishna Mohan, B. Mechanical Properties of High-Strength Micro Steel Fibre Reinforced Concrete Subjected to High Temperatures. *Mater. Today Proc.* 2023, *in press*. [CrossRef]
60. Ünverdi, M.; Bayqra, S.H.; Kaya, Y.; Özen, S.; Mardani, A.; Ramyar, K. Mechanical Performance, Statistical Optimization, and Environmental Impact of Roller-Compacted Concrete Reinforced with Waste and Industrial Fibers. *Buildings* **2026**, *16*, 1167. [CrossRef]
61. Mardani, A.; Hatungimana, D.; Mardani, N.; Assaad, J.; El-Hassan, H. Feasibility of Steel Fiber-Reinforced Self-Compacting Concrete Containing Recycled Aggregates–Compliance with EFNARC Guidelines. *Int. J. Sustain. Eng.* **2025**, *18*, 2538858. [CrossRef]
62. Koksal, F.; Kocabeyoglu, E.T.; Gencel, O.; Benli, A. The Effects of High Temperature and Cooling Regimes on the Mechanical and Durability Properties of Basalt Fiber Reinforced Mortars with Silica Fume. *Cem. Concr. Compos.* **2021**, *121*, 104107. [CrossRef]
63. Öz, A.; Bayrak, B.; Aydın, A.C. The Effect of Trio-Fiber Reinforcement on the Properties of Self-Compacting Fly Ash Concrete. *Constr. Build. Mater.* **2021**, *274*, 121825. [CrossRef]
64. Aydin, S.; Baradan, B. Effect of Pumice and Fly Ash Incorporation on High Temperature Resistance of Cement Based Mortars. *Cem. Concr. Res.* **2007**, *37*, 988–995. [CrossRef]
65. Khaliq, W.; Kodur, V. High Temperature Mechanical Properties of High-Strength Fly Ash Concrete with and without Fibers. *ACI Mater. J.* **2012**, *109*, 665–674. [CrossRef]
66. Hager, I.; Sitarz, M.; Mróz, K. Fly-Ash Based Geopolymer Mortar for High-Temperature Application—Effect of Slag Addition. *J. Clean. Prod.* **2021**, *316*, 128168. [CrossRef]
67. Sarıdemir, M.; Bulut, M.; Deniz, S.; Deneme, İ.Ö. Long-Term Properties of Steel Fiber Reinforced Silica Fume Based AAMs at Ambient and High Temperatures. *Constr. Build. Mater.* **2024**, *416*, 135046. [CrossRef]
68. *EN 197-1*; Cement—Part 1: Composition, Specifications and Conformity Criteria for Common Cements. EN Standards: Newark, DE, USA, 2015.
69. *ASTM C618-22*; Standard Specification for Coal Fly Ash and Raw or Calcined Natural Pozzolan for Use in Concrete. ASTM International: ASTM International: West Conshohocken, PA, USA, 2022.
70. *EN 1097-1*; Tests for Mechanical and Physical Properties of Aggregates—Part 1: Determination of the Resistance to Wear. EN Standards: Newark, DE, USA, 2023.
71. *ASTM C109/C109M-24*; Standard Test Method for Compressive Strength of Hydraulic Cement Mortars. ASTM International: West Conshohocken, PA, USA, 2025.
72. *ASTM C1437-20*; Standard Test Method for Flow of Hydraulic Cement Mortar. ASTM International: ASTM International: West Conshohocken, PA, USA, 2020.
73. *EN 196-1*; Methods of Testing Cement—Part 1: Determination of Strength. EN Standards: Newark, DE, USA, 2018.
74. *ASTM C597-22*; Standard Test Method for Ultrasonic Pulse Velocity Through Concrete. ASTM International: ASTM International: West Conshohocken, PA, USA, 2022.
75. *ASTM C642-21*; Standard Test Method for Density, Absorption, and Voids in Hardened Concrete. ASTM International: West Conshohocken, PA, USA, 2022.
76. Meng, W.; Valipour, M.; Khayat, K.H. Optimization and Performance of Cost-Effective Ultra-High Performance Concrete. *Mater. Struct./Mater. Constr.* **2017**, *50*, 29. [CrossRef]
77. Van Den Heede, P.; De Belie, N. Environmental Impact and Life Cycle Assessment (LCA) of Traditional and "green" Concretes: Literature Review and Theoretical Calculations. *Cem. Concr. Compos.* **2012**, *34*, 431–442. [CrossRef]
78. Gao, D.; Zhang, W.; Tang, J.; Zhu, Z. Effect of Steel Fiber on the Compressive Performance and Microstructure of Ultra-High Performance Concrete at Elevated Temperatures. *Constr. Build. Mater.* **2024**, *435*, 136830. [CrossRef]
79. Zhang, Y.; An, Z.; Zhao, W.; Hao, Z.; Sun, G.; Yan, Z.; Ju, J.W. Post-High-Temperature Performance of Multi-Scale Fiber Reinforced UHPC: The Role of Steel Fiber Type in Toughness and Pullout Behavior. *J. Build. Eng.* **2025**, *111*, 113465. [CrossRef]
80. Afroughsabet, V.; Biolzi, L.; Ozbakkaloglu, T. High-Performance Fiber-Reinforced Concrete: A Review. *J. Mater. Sci.* **2016**, *51*, 6517–6551. [CrossRef]

81. Chu, S.H.; Kwan, A.K.H. Co-Addition of Metakaolin and Silica Fume in Mortar: Effects and Advantages. *Constr. Build. Mater.* **2019**, *197*, 716–724. [CrossRef]
82. Flower, D.J.M.; Sanjayan, J.G. Greenhouse Gas Emissions Due to Concrete Manufacture. *Handb. Low Carbon Concr.* **2017**, *12*, 1–16. [CrossRef]
83. Ali, B.; Qureshi, L.A.; Kurda, R. Environmental and Economic Benefits of Steel, Glass, and Polypropylene Fiber Reinforced Cement Composite Application in Jointed Plain Concrete Pavement. *Compos. Commun.* **2020**, *22*, 100437. [CrossRef]

Disclaimer/Publisher's Note: The statements, opinions and data contained in all publications are solely those of the individual author(s) and contributor(s) and not of MDPI and/or the editor(s). MDPI and/or the editor(s) disclaim responsibility for any injury to people or property resulting from any ideas, methods, instructions or products referred to in the content.